

IR 80-2062

EA-6010-23

Dist. Category UC-90C

MATERIALS RESEARCH FOR THE CLEAN UTILIZATION OF COAL

QUARTERLY PROGRESS REPORT

January - March 1980

Samuel J. Schneider  
Project Manager

Center for Materials Science  
National Bureau of Standards  
U. S. Department of Commerce  
Washington, D. C. 20234

PREPARED FOR THE UNITED STATES  
DEPARTMENT OF ENERGY

Office of Advanced Research and Technology

Under Contract No. EA-77-01-6010

"This report was prepared as an account of work sponsored by the United States Government. Neither the United States nor the United States Department of Energy, nor any of their employees, nor any of their contractors, subcontractors, or their employees, makes any warranty, expressed or implied, or assumes any legal liability or responsibility for the accuracy, completeness, or usefulness of any information, apparatus, product or process disclosed, or represents that its use would not infringe privately owned rights."

## TABLE OF CONTENTS

|                                                         | PAGE |
|---------------------------------------------------------|------|
| I. SUMMARY OF PROGRESS TO DATE . . . . .                | 1    |
| II. DETAILED DESCRIPTION OF TECHNICAL PROGRESS. . . . . | 3    |
| 1. Materials Performance and Properties . . . . .       | 3    |
| 2. Creep of MHD Refractories. . . . .                   | 5    |
| 3. Electrical Transport Mechanisms in Slag. . . . .     | 7    |
| 4. Corrosion of Downstream MHD Components . . . . .     | 15   |

# I. SUMMARY OF PROGRESS TO DATE

## Brief Summary

### 1. Materials Performance and Properties

An interpretive report, summarizing erosive wear failures in coal conversion pilot plants was completed, reviewed by DOE and submitted for NBS editorial review. The Failure Information Center transmitted 198 abstracts and 8 hard-copy reports to industry. Benchmark testing of candidate computer software vendors was completed during the quarter and additional progress was made in completing the first draft of sections of the Construction Materials Handbook for Coal Gasification.

### 2. Creep of MHD Refractories

Compressive yield measurement at 1400 °C, 1500 °C, and 1580 °C are presented for loading at 0.0002 in/min. The status of the 12 station creep assembly is presented.

### 3. Electrical Transport Mechanisms in Slag

The electrical conductivity of  $YCrO_3$  doped with five percent Ca has been measured in a highly reducing atmosphere at temperatures from 1300 to 1600 °C. The samples are not single phase in composition, however, and this may have caused some errors in the bulk conductivity values due to hair-line cracks or phase boundaries.

Several polarization experiments have been completed using slag (Bow, New Hampshire) as an electrolyte and using platinum electrodes. These were made in a specially designed cell incorporating four probes to allow polarization to be measured at any probe as a function of time at a given temperature and for a preset condition regarding charge transfer (constant current or constant voltage).

The electrical conductivity of a Bow, New Hampshire, slag sample containing an added amount of iron has been measured. At low temperatures (1200 °C) the conductivity increased nearly proportional to the added iron but at higher temperatures (above 1350 °C) the conductivity increased by a factor of five when the iron content was doubled. This increase in conductivity may be due to the decrease in viscosity associated with iron addition and/or equivalent silica decrease.

#### 4. Corrosion of Downstream MHD Components

Type 316 stainless steel tubes, cooled to 400 °C, 500 °C, and 590 °C, were exposed to oxygen-rich hot gas streams seeded with  $K_2SO_4$ . Optical SEM, and EDX analysis indicate the geometric and chemical nature of the deposits and reaction zones to be similar to those of Type 304 stainless steel exposed previously under the same conditions. As in those cases, Fe appears to have penetrated the farthest into the salt deposit region while the dispersion of Ni in the reaction zone area remains the most difficult to follow. The extent of wastage (weight loss) of Type 316 and Type 304 stainless steel exposed at 590 °C and 400 °C to  $K_2SO_4$  seeded oxygen-rich hot gas streams was also determined.

In the coming quarter further exposure tests will be conducted on Type 304 and Type 316 stainless steels to determine wastage under oxygen-rich conditions with a seed of 80 percent by weight  $K_2CO_3$  and 20 percent by weight  $K_2SO_4$ .

## II. DETAILED DESCRIPTION OF TECHNICAL PROGRESS

1. Materials Performance and Properties (H. M. Ondik, R. C. Dobbyn, A. Perloff, W. S. Brower, and W. A. Willard)

Progress: Collection and evaluation of materials performance and properties data continued during the quarter.

An interpretive report, analyzing erosive wear failures of pilot plant components was completed and submitted to DOE for comment and approval. The report entered the NBS editorial review process in March after receipt of the sponsor's approval.

The Failure Information Center also handled six requests for information; a total of 198 abstracts and eight hard-copy reports were transmitted in response to these requests. The Center also received several visitors during this period. A current failure mode analysis by component type is given in Table 1.

Project staff have spent most of this quarter extracting, evaluating, and tabulating data for Section B (Materials Evaluation Test Data) of the Construction Materials Handbook. Approximately seventy-five percent of this section has been completed. The compilation and evaluation of some data has been purposely postponed in anticipation of final reports.

Benchmark evaluation of candidate suppliers of the software package for the new Materials Performance and Properties Data Base was completed during the quarter. The Department of Commerce ADP procurement office will soon set a date for contractors' submission of "best and final" cost proposals; selection of a software supplier will follow.

Plans: Completion of Sections A and B of the Construction Materials Handbook is scheduled for the next quarter. Normal data acquisition activities will continue. The interpretive report on erosive failures in pilot plants will be submitted for publication as an NBS Internal Report; publication as a DOE report is recommended. Selection of a software contractor for the data base is also expected to be completed during the next quarter.

TABLE 1

NATIONAL BUREAU OF STANDARDS  
FAILURE INFORMATION CENTER

FAILURE MODE ANALYSIS

| FAILURE MODE      | COMPONENT       |                 |          |          |          |            |
|-------------------|-----------------|-----------------|----------|----------|----------|------------|
|                   | AUX<br>EQUIP(1) | COAL<br>HAND(2) | PIPING   | PUMPS    | VALVES   | VESSELS(3) |
| CORROSION         | 14              | 1               | 56       | 4        | 8        | 13         |
| DESIGN            | 9               | 0               | 3        | 9        | 7        | 7          |
| EROSION           | 6               | 0               | 28       | 19       | 19       | 3          |
| EROSION/CORROSION | 3               | 0               | 4        | 5        | 0        | 1          |
| FABRICATION       | 0               | 0               | 6        | 0        | 1        | 0          |
| PROCESS CONTROL   | 18              | 6               | 22       | 9        | 9        | 7          |
| QUALITY CONTROL   | 4               | 1               | 1        | 0        | 3        | 0          |
| SCC               | 0               | 0               | 21       | 0        | 2        | 6          |
| SCC-CL            | 0               | 0               | 22       | 0        | 0        | 2          |
| STRESS/TEMP       | 6               | 1               | 12       | 4        | 1        | 12         |
| UNKNOWN           | 7               | 2               | 10       | 7        | 5        | 1          |
| WEAR              | <u>3</u>        | <u>1</u>        | <u>0</u> | <u>5</u> | <u>6</u> | <u>0</u>   |
|                   | 70              | 12              | 185      | 62       | 61       | 52         |

(1) INCLUDES COMPRESSORS, CYCLONES, THERMOCOUPLES, AND OTHERS

(2) INCLUDES BAGHOUSE, FILTERS, CONVEYORS, ELEVATORS, AND OTHERS

(3) INCLUDES GASIFIERS, REGENERATORS, DISSOLVERS, SEPARATORS, AND OTHERS

TOTAL NUMBER OF INCIDENTS = 442

2. Creep and Related Properties of MHD Refractories (N. J. Tighe and  
C. L. McDaniel, 562)

Progress: Work during the quarter was directed toward 1) assembling the 12 creep stations, and 2) acquiring data on the compressive yield of the magnesia-rich spinel refractory X-317.

Experimental Procedure: Compressive yield measurements were made on core samples obtained from R. Smyth of Fluidyne. The cores were machined to 3 in long with a 1 in long by 1/2 in diameter reduced cross-section. The compressive yield experiments were carried out using a constant loading rate of 0.0002 in/min at temperatures of 1400 °C, 1500 °C, and 1600 °C.

Results:

Creep Station: The four furnaces for the creep station were delivered in late December. The furnaces have been sited and the load cells and pneumatic loading fixtures for the 12 stations were mounted on the frames. The furnace assemblies are shown in Figures 1a and 1b. Drive rods and water-cooled rod holders are being machined.

Compressive Yield: The X-317 refractory was shown to be relatively creep-resistant in our earlier reports and in the reports from Fluidyne. From the compressive yield measurements we can obtain the limiting conditions for application of dead-weight creep. The measurements are planned for three loading rates with three specimens at each loading rate. The first results at 0.0002 in/min are as follows:

|                            | <u>1400 °C</u> | <u>1500 °C</u> | <u>1580 °C</u> |
|----------------------------|----------------|----------------|----------------|
| Stress at yield drop, ksi  | 8.5            | 8.0            | 6.0            |
| Total Deformation, percent | 2.3            | 3.9            | 1.7            |
| Time at constant load, hr. | 2.0            | 2.5            | 1.0            |

Plans: The creep stations should be completed during the next quarter and long-term creep tests can be started. The relevance of the present choice of materials for the creep tests will be discussed with members of the MHD materials group. A paper covering the results of our creep tests and micro-structural analysis of the chrome-magnesite refractory designated RFG will be presented at the Annual Meeting of the American Ceramic Society in April 1980.

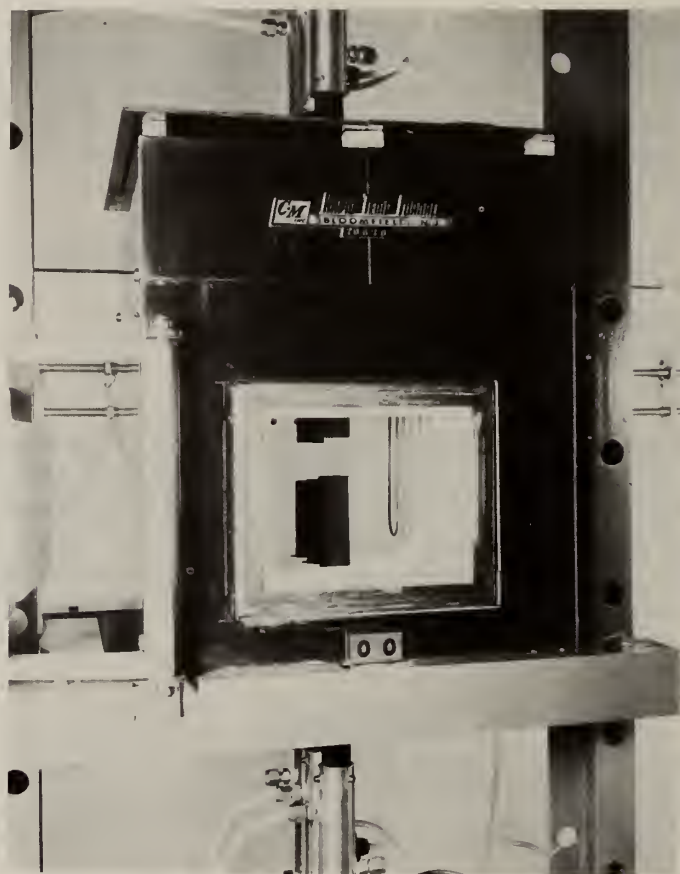


Figure 1. The 12 station creep assembly showing: (a) arrangement of the four furnaces, (b) arrangement of the loading furnace, and load cells.

### 3. Electrical Conductivity and Polarization (W. R. Hosler)

#### Progress:

#### a. Electrical Conductivity of $\text{YCrO}_3$

Initial measurements of the pressure dependence of the electrical conductivity of  $\text{YCrO}_3$  doped with five percent calcium on the yttrium site have been completed. There has been some difficulty in establishing the oxygen partial pressure in the sample chamber that corresponds to the oxygen partial pressure in the flowing gas where oxygen/nitrogen gas mixtures are used. This difficulty arises because of the large sample chamber ( $1200 \text{ cm}^3$ ) originally filled with air which must be swept out with the flowing environment gas of chosen composition. True oxygen pressure dependence of the conductivity can only be measured after the environment gas has been completely changed in the sample chamber. This requires times in excess of four hours with a flow rate of  $450 \text{ cm}^3/\text{minute}$ . In contrast, however, for those atmospheres where very low oxygen pressures are obtained by the reaction  $2\text{H}_2 + \text{O}_2 \rightarrow 2\text{H}_2\text{O}$  such as is obtained using forming gas (95 nitrogen to 5 hydrogen), the low oxygen pressures are obtained quickly (1 hour or less) in the environmental chamber. The measurements have been completed in atmospheres containing about  $5 \times 10^{-6}$  atmosphere  $\text{O}_2$  in one atmosphere  $\text{N}_2$  and in  $10^{-25}$  atmosphere  $\text{O}_2$  as indicated on a zirconia tube oxygen sensor gauge based on the Nernst-Einstein relation. (Intermediate oxygen pressures between  $5 \times 10^{-6}$  and  $10^{-25}$  atmospheres will be obtained in future experiments by mixing the 5 ppm gas with forming gas.)

Table 1 gives values of conductivity ( $\sigma$ ) and soak temperatures. The conductivity values are those taken at the end of the soak period, but data were taken at five to ten minute intervals during the soak period, while equilibrium was being established. The order in the Table is the sequence in which the data were taken. As can be seen, the scatter in the conductivity data is quite large.

Table 1

| <u>Temp. °C</u> | <u><math>\text{O}_2</math> pressure (atmos.)</u> | <u>Elec. Conduct (ohm-cm)<sup>-1</sup></u> | <u>Total flow time before meas. (hr)</u> | <u>Soak Time at T. (hr)</u> |
|-----------------|--------------------------------------------------|--------------------------------------------|------------------------------------------|-----------------------------|
| 1300            | $5 \times 10^{-6}$                               | 2.9                                        | 18                                       | 18                          |
| 1500            | "                                                | 3.12                                       | 20                                       | 2.5                         |
| 1400            | "                                                | 3.05                                       | 23.5                                     | 3.0                         |
| 1400            | $5 \times 10^{-25}$                              | 1.05                                       | 11.5                                     | 11.5                        |
| 1600            | "                                                | 1.30                                       | 14.5                                     | 3.0                         |
| 1500            | "                                                | 1.05                                       | 16                                       | 1.5                         |
| 1400            | "                                                | 0.92                                       | 17                                       | 1.0                         |
| 1300            | "                                                | 1.04                                       | 36.5                                     | 19.5                        |
| 1600            | "                                                | 1.02                                       | 45.0                                     | 8.5                         |
| 1500            | "                                                | 0.88                                       | 56.5                                     | 11.5                        |

There has been some difficulty in preparing good single phase material. Possibly as a result of this multiphase condition samples sometimes exhibited small hairline cracks when they were oxidized after being prepared in a highly reduced state. These cracks would cause erratic results in the conductivity values.

$\text{YCrO}_3$  doped with Ca or Mg in a highly reduced state is very hard and it is difficult to saw or drill with diamond tools. In the oxidized state, however, it is relatively soft and sometimes fragile and breaks easily upon handling. More work must be done on phase composition and microstructure and their relation to oxidation/reduction conditions before final work can continue on the associated electrical conductivity.

#### b. Electrochemical Effects of Slag-Electrode Interfaces

An electrochemical cell consisting of four platinum probes immersed in Bow, New Hampshire, slag containing 20 percent added  $\text{K}_2\text{SO}_4$  was constructed. This cell was heated to 1250 °C and subjected to a constant applied voltage mode test where the voltage was reversed periodically during the course of a 2½ hour run. Voltages were monitored on all probes during the test.

Figure 1 is a radiograph of the electrochemical cell, while Figure 2 shows the voltage on the various probe sets as a function of time. A constant 31 volts was maintained between the top and bottom probes and this resulted in an initial current after each current reversal of 60 to 100 mA which drops off with time as shown in the figure. The current was reversed at five minute intervals (after an initial interval of 2½ minutes) over a period of 2½ hours. Only 23½ minutes of the data are shown, but the remaining data over the entire experiment period are repetitive. It can be readily seen, for example, that when the top probe is positive (anode) as in periods A, C, and E, nearly all the potential drop in the cell is across the  $I_T \rho_T$  set of probes after a few minutes operation, while the voltage across  $I_B \rho_B$  ( $I_B$  cathode) is low. Current reversal then as in periods B and D, ( $I_B$  (anode),  $I_T$  (cathode)) shows the potential drop large at the  $I_B \rho_B$  probes and small at the  $I_T$  probes. In previous experiments (see QR Sept.-Dec. 1977), some iron depletion was observed in the anode area just outside the platinum electrode in an electrochemical cell run for a period of 20 hours at 1400 °C. At the same time, definite enrichment of iron was observed at the cathode slag-electrode interface. Cadoff<sup>(1)</sup> in electrochemical work on slag-electrode reactions shows that in cells designed for static slag (non-flowing), the potential buildup of the cell is due to the accumulation of electrically resistive ions at the slag/anode interface. Koester et al<sup>(2)</sup>, have shown that the critical potential for arcing or breakdown is higher for 1018 steel than for nickel or 304 stainless steel. This may be due to the supply of iron from the anode electrode alleviating the usually iron poor (or silica rich) area just at the anode/slag boundary usually associated with an electrode material not containing iron. This experiment demonstrates that this potential buildup is relatively rapid

and is associated with the slag-anode interface. At the same time, the conductivity of the bulk slag remains unchanged, since the potential on the probes  $\rho_T$   $\rho_B$  drops off in proportion to the drop off in the primary current while the applied voltage is constant.

A second experiment on this same cell was performed using a constant current (30 mA) mode but reversing the current periodically (five minute intervals). Figure 3 shows that data obtained over a 20 minute period in the experiment. Although the experiment was run for 1½ hours, only slight changes were observed with time on reversal of the current. Breakdown in the current conducting mechanisms after a current reversal appears to occur earlier when the  $I_B$  probe is an anode as in period B and D (1.5 to 2.0 minutes) than when the  $I_T$  probe is an anode as in periods A and C (four to five minutes). Since the experiment was run at 1250 °C, there could be a difference in the oxidation state of the iron between the top and bottom of the cell and this might cause a difference in the breakdown potential when the anode is at the bottom of the cell (away from ambient atmospheres). Also with the top of the cell as anode for a five minute period followed by a five minute period with the current off (these periods not shown in figure) the cell returns to its original state, i.e., the potentials are distributed evenly along the length of the cell showing that any depletion layer has been repaired. However, with the bottom of the cell as anode, and the same procedure followed, the depletion layer is not repaired completely even after a period of 50 minutes. A measurement of all probe voltages with current off yields zero potential indicating that there is no measurable battery effect present. In this constant current mode, the high potential develops between the anode and its adjacent conductivity probe as was also observed in the constant voltage mode. Breakdown occurs also at the anode. The corresponding cathode potential decreases with time after a slight initial increase after reversal. The slag bulk conductivity decreased (potential on  $\rho$  probes increased) slightly during the course of the experiment which may be due to iron diffusion into the platinum electrodes.

Both of these experiments were done at a temperature (1250 °C) where the slag is very viscous and where there may be a combination of ionic and electronic (semiconductive) conductivity. If time permits, this experiment should be repeated at higher temperatures where the conductivity is believed to be largely ionic and due primarily to the movement of iron ions. (3)

### c. Slag Electrical Conductivity

A sample of slag was made from the Bow, New Hampshire, slag which contained an added 20 percent  $K_2SO_4$ , but now with an additional 20 percent of  $Fe_2O_3$ . Figure 4 shows the conductivity data as a function of temperature in an air atmosphere. The sample was heated to 1500 °C and held at the temperature until the conductivity became constant as a function of time (< ½-hour). It was then cooled as rapidly as possible in the furnace to 900 °C which required a period of 24 minutes. The temperature was then lowered slowly to 500 °C. The data shown in Figure 4 were taken with increasing temperature

and at each temperature point, conductivity vs. time was monitored to obtain maximum or minimum conductivity values. The conductivity is higher in this sample than in its companion sample without the added iron (shown in QR July - Sept., 1979). The conductivity near the maximum at 1200 °C is approximately a factor of two higher in this sample with the added iron when long times are allowed for crystallization of the slag in this temperature range. X-ray diffraction measurements indicate that at these conductivity maxima, the crystalline components of the slag are feldspar, sesquioxide, and spinel solid solutions of undefined bulk compositions. It is not possible to deduce whether the conductivity is due to these crystalline phases or to an iron-rich glassy matrix likely to be surrounding the crystalline components. In the latter case, the conductivity would be predominantly ionic. However, polarization effects were not observed in this temperature range during the electrical measurement.

The conductivity in the higher temperature range above 1350 °C is a factor of five greater in this sample with added iron (24.2 w/o) than in the sample with no added iron (14.7 w/o). Capps<sup>(4)</sup> has shown that there is a decrease in slag viscosity with increased iron content and with decreased silica content. The relative silica content necessarily decreases with any added component other than silica itself. This disproportionate increase in conductivity may be due to the viscosity decrease reflecting the validity of the Walden rule<sup>(5)</sup> i.e.,  $\eta \cdot \sigma = \text{const.}$  where  $\eta$  is viscosity and  $\sigma$  is the electrical conductivity for conducting ionic species (iron ions) in a molten glass.

Plans: The electrochemical experiments will continue with the experiments described in the report repeated at higher temperatures in order to determine the polarization and relaxation times associated with any depletion layer formed while the cell is carrying current.

Work on the slag electrical conductivity will continue also. Preliminary investigations indicate that adding iron as  $\text{Fe}_2\text{O}_3$  or  $\text{Fe}_3\text{O}_4$  to Bow, New Hampshire, slag without potassium causes excessive frothing and that these additions can only be made in a highly reducing atmosphere. Additional transition element dopings may be investigated in order to better understand the conductivity.

### References

- (1) Westinghouse Electric Corporation--Quarterly Report for the Period Oct. 1 to Dec. 31, 1977, Contract No. EX-76-C-01-2248.
- (2) Electrical Behavior of Slag Coatings in Coal Fired MHD Concentrations, J. K. Koester and R. M. Nelson, 16th Symposium on Engineering Aspects of Magnetohydrodynamics, University of Pittsburgh, Pittsburgh, Pennsylvania, May 16-18, 1977.
- (3) Conductivity Mechanisms in Iron-Containing Slag, W. R. Hosler, G. S. White, and T. Negas - 7th International Symposium on MHD, M.I.T., Cambridge, Massachusetts, June 16-20, 1980.

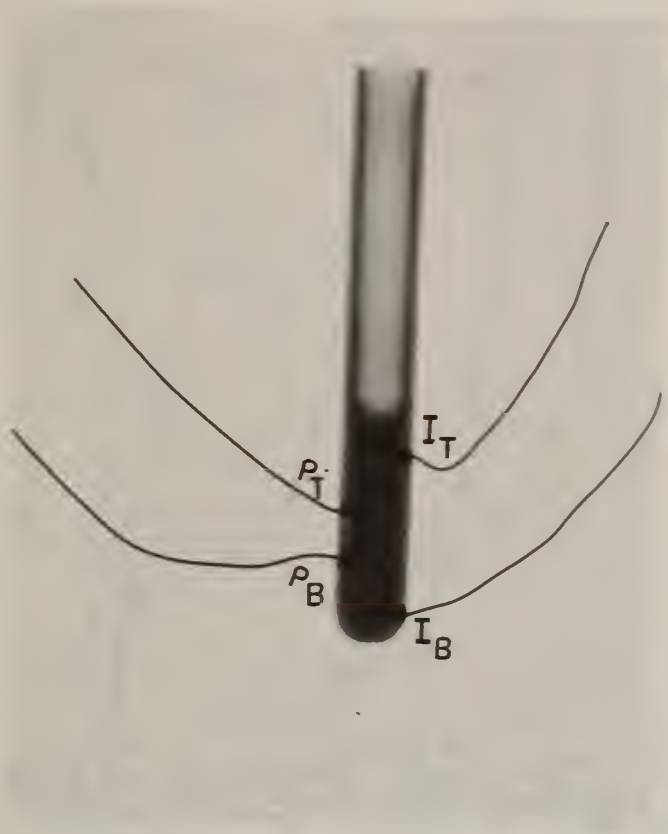


Figure 1. Radiograph of the electrochemical cell showing the arrangement of the platinum electrodes.

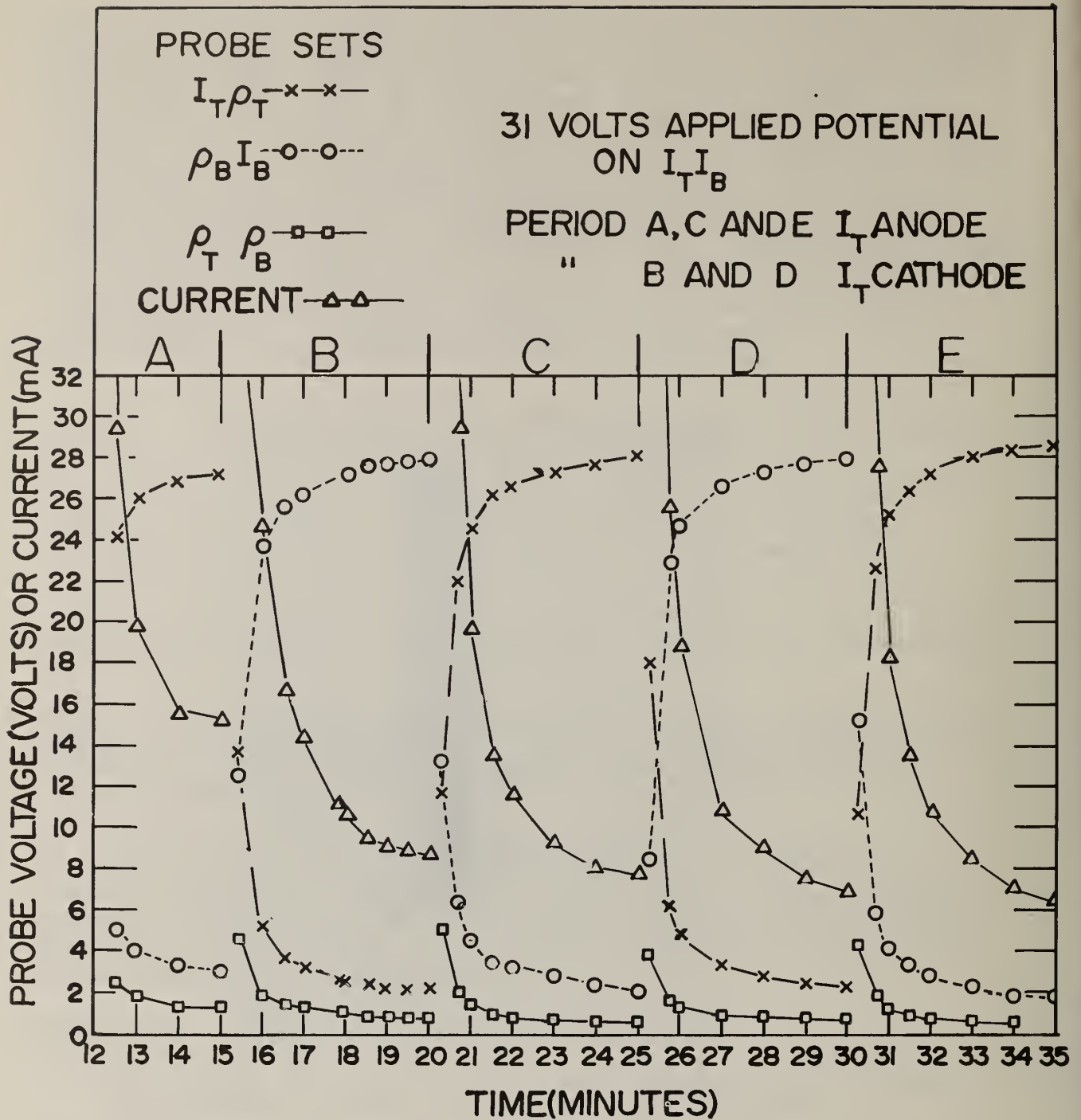


Figure 2. Probe set voltages and current as a function of time with periodic applied voltage polarity reversal. The applied voltage magnitude was constant during the run. Cell temperature 1250 °C.

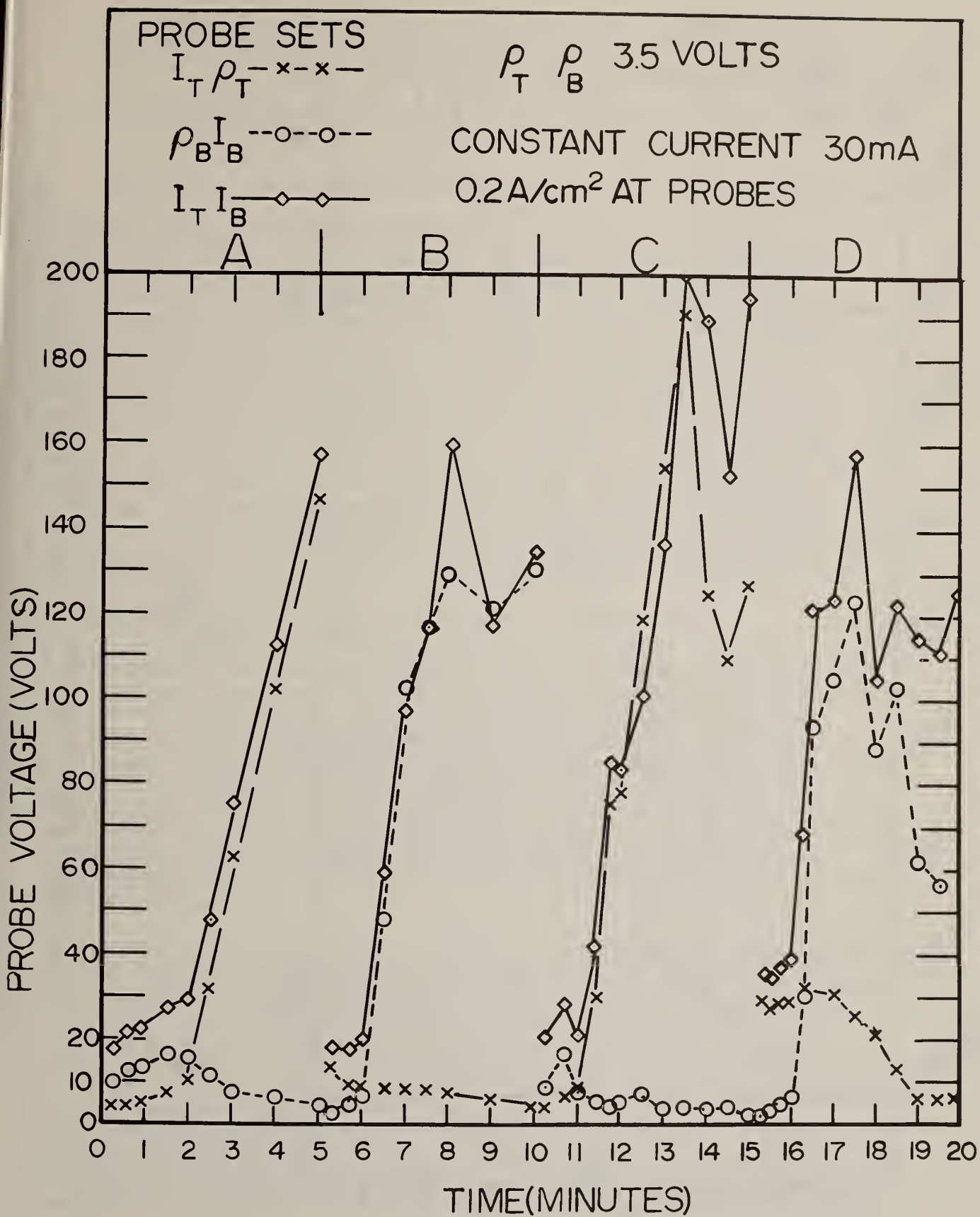


Figure 3. Probe set voltages as a function of time with periodic applied voltage polarity reversal. The current magnitude was constant during the run. During breakdown, recorded voltage magnitudes do not represent systematic cell behavior. Period A and C,  $I_T$  was anode. Period B and D,  $I_B$  was anode. Cell temperature 1250 °C.

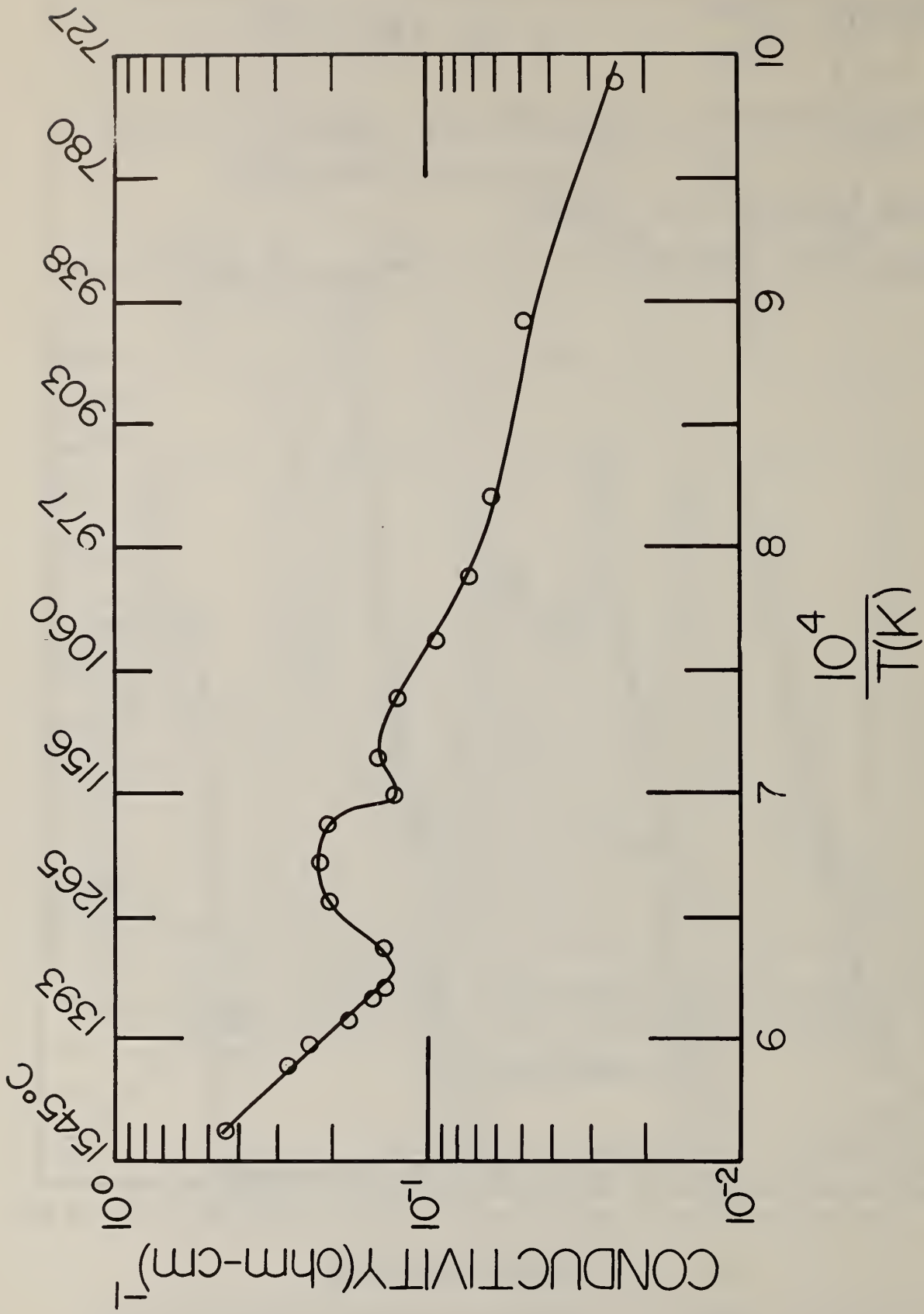


Figure 4. Electrical conductivity of Bow, NH slag with an added 20 w/o  $K_2SO_4$  and with 34.6 w/o  $Fe_2O_3$  (24.3 w/o Fe) as a function of temperature. These measurements were done in air.

- (4) Coal Slag Properties Related to MHD, W. Capps, Conference on High Temperature Sciences Related to Open-Cycle Coal Fired MHD Systems, Argonne National Laboratory, Argonne, Illinois, April 4-6, 1977.
- (5) International Review of Science--Electrochemistry-Physical Chemistry Series Two, Volume 6, J. Bocknis, Editor, p. 290 (1976).

#### 4. Corrosion of Downstream MHD Components (J. Smit and C. D. Olson)

Progress: Tubular specimens of Type 316 and Type 304 stainless steel were exposed, under varied conditions, to  $K_2SO_4$  seeded, oxygen-rich, oxygen-propane hot gas streams. Following exposure, the specimens were analyzed using SEM, EDX, and, in some cases, gravimetric techniques for indications of both incipient and gross corrosion. Test exposure times, excluding apparatus warm-up and cool down time, was four hours. Seeding with 250 grams of  $K_2SO_4$  was effected during the first 25 minutes of that interval. Six stainless steel specimens were exposed under these general conditions with the tube temperature maintained at one of three levels: 400 °C, 500 °C, or 590 °C. These temperatures were fixed by internal air cooling and were monitored by a Pt/Pt 10 percent Rh thermocouple welded into the specimen wall at the mid-length point. The specimens were seated in the test rig with the thermocouple located in the center of the hot zone and facing the gas stream. The gas stream temperature in the vicinity of the test specimen was held at approximately 1300 °C as indicated by a Pt/Pt 10 percent Rh thermocouple.

##### a. SEM/EDX Analysis of the Metal-Deposit Interface

Metallographic specimens were prepared from three of the Type 316 stainless steel specimens, 1-6, 2-6, and 3-6, exposed at 590 °C, 500 °C, and 400 °C, respectively. These sections were taken approximately 10 mm from the mid-point position in the hot zone. To reduce the possibility of external contamination and hydration in the coatings formed on the tubular specimens during seeding, the specimens were removed from the test rig upon cool down to about 40 °C and encapsulated immediately in epoxy. The metallographic sections taken from the encapsulated tubular specimens were cut, ground, and polished using non-aqueous media and were stored in evacuated desiccators prior to SEM/EDX analysis.

On all the specimens, a compact, somewhat columnar deposit formed on the surface facing the gas stream. The thickness of this deposit varied slightly with tube temperature and is approximately 1.7 mm. A much thinner, almost undetectable deposit, probably from fume, formed on the trailing surface. These deposits are in the 0.2 mm range. At the boundary, where the surface deposit and the fume deposit intersected a thicker drip zone formed, see Figs. 1, 2 and 3. SEM micrograph, Fig. 4, shows a  $K_2SO_4$  deposit on the leading surface of a Type 316 stainless steel tube held at 590 °C. This type of deposit is typical of that produced from  $K_2SO_4$  seeding and was seen on specimens of Type 304 stainless steel tested previously under these conditions. EDX analysis indicates that potassium and sulfur is uniformly distributed through

the bulk of the deposit. SEM micrograph, Fig. 5, shows the top of the salt deposit with a fine whitish band on the surface. This band contains a higher proportion of potassium than the bulk of the deposit possibly due to vaporization of some sulfur at the deposit-gas stream interface. The stainless steel deposit interface is seen in SEM micrograph, Fig. 6. Note that the adhesion is rather poor as epoxy fills a gap in the interface region. A reaction area at the interface is shown in SEM micrograph, Fig. 7. At the metal edge, areas of low chromium and low nickel concentration are found dotted with regions of high nickel concentration, Figs. 7a - 7d. A loss of iron is also associated with these areas. At the deposit edge, concentrations of iron, chromium, potassium, and sulfur are found indicating some degradation of the metal surface and formation of a reaction zone between the metal and the deposit, Figs. 7e - 7h. The SEM/EDX analysis seems to indicate a preferential leaching of the metal cations from the bulk material (Type 316 stainless steel) in a somewhat orderly fashion as in the case of Type 304 stainless steel. However, the extent of corrosion is not as great as in the case of Type 304 stainless steel. This is corroborated by wastage (weight loss) experiments also described in this report.

As found in previous specimens, though nickel loss is readily detected, its displacement to other areas is difficult to follow. Few areas are found where nickel has migrated even though its concentration is low. Fig. 8 shows a reaction area where low chromium and low nickel concentration are found at the metal edge, Figs. 8a and 8b, and metal cations are found at the edge of the deposit, Figs. 8c - 8e. Migration of the iron, Fig. 9, is farther back in the deposit and generally parallels previous results in which iron was preferentially leached out of the bulk stainless steel and into the deposit.

Fig. 10 shows a portion in the fume deposit area where the corrosion process seems to be evident. On the metal edge low nickel areas are found, Figs. 10a - 10c, while areas of chromium, iron, potassium, and sulfur are found in the reaction zone. Again nickel is the elusive element. Though it is found in low concentration in the reaction zone, it is not really found to have migrated into the deposit region.

At a lower temperature, 500 °C, corrosion is still observed in Type 316 stainless steel. Fig. 11 shows a region of corrosion at the metal-deposit interface. EDX analysis of the region, Figs. 11a - 11h, indicate areas of low metal cation concentration at the metal edge and metal cation migration into the deposit. The same can be said at the still lower specimen temperature of 400 °C but to a much lesser extent.

#### b. Metal Wastage Analysis

Weight loss determinations and tube surface examinations by SEM and EDX techniques were also made on Type 316 and Type 304 stainless steels. Three specimens, one of Type 316 stainless steel, specimen 4-6 and two of Type 304 stainless steel, specimens 13-4 and 14-4, were weighed

prior to exposure at tube wall temperature of 590 °C, 590 °C, and 400 °C, respectively, under the general conditions as described in the first paragraph of this report. In these cases after extraction from the test rig the entire specimen was rinsed in warm water and subsequently cleaned in ten percent HNO<sub>3</sub> at 50 °C for 20 minute cycles in an ultrasonic bath until constant weight was obtained. In each case the second cleaning cycle resulted in no further detectable weight change. The differences in weight (weight loss) are attributed to loss of metal (wastage) from the specimen, see Table 1. Figs. 12, 13 and 14 show the stainless steel tubes after exposure and cleaning. After weighing, sections were taken from each tube for SEM/EDX analysis.

Fig. 15 is a micrograph of specimen 4-6 which shows areas of pitting and wastage. Fig. 16 along with the EDX analysis indicate regions of cation migration and concentration. There seems to be no general trend toward concentration of any metal cation; however, there seems to be a general trend toward lower nickel concentrations. To see if these conclusions were reasonable, another area, shown in Fig. 17, was examined. Fig. 18 shows again areas of low nickel, Fig. 18a and 18b, but also regions of high nickel, Fig. 18c, along with areas of other metal cation concentration. However, the high nickel regions are generally isolated and not in sufficient number to account for all the low nickel regions. Although the wastage (weight loss) of this sample was minimal, the nickel concentration tends to be lower than that of the bulk stainless. Possible explanations for this would be either that the nickel is being attacked and lost through some volatile chemical reaction or that there is a formation of a higher chromium, iron layer that has migrated upward covering the nickel. In either case, lower nickel would be observed.

In samples 13-4 and 14-4 a comparison evaluation can be made of the same type of stainless steel exposed at two different temperatures. The greatest change in weight (wastage) was observed in sample 13-4, while a minimal amount was lost in sample 14-4, see Table 1. Fig. 19 exhibits an area of sample 13-4 riddled with holes and depressions between grains. Figs. 20, 20a - 20f show metal cation concentration or loss in this area.

In sample 14-4 grain boundaries and grain forms are evident, see Fig. 21; however, there are not as many pores or holes showing. Black spot regions, though, are prevalent on the grain surfaces. Fig. 22 shows these areas rather vividly; SEM/EDX analysis indicates them to be areas of low chromium, low nickel, and high iron concentration associated with potassium and sulfur. These areas are probably the beginning of reaction sites on the stainless steel surface. Fig. 23 is a high magnification micrograph of one such spot. EDX analysis, Figs. 23a and 23b, indicate low chromium and low nickel along with potassium and sulfur in that spot with high metal cation concentration surrounding blackish area.

A random sample of 304 stainless steel was selected for SEM/EDX analysis and used as a comparison to the specimens placed in the corrosive environment. Prior to sectioning the sample was cleaned with 10 percent HNO<sub>3</sub> at 50 °C for 20 minute cycles in an ultrasonic bath. A comparison of this surface to the surfaces exposed to the corrosive environment

shows that while grain boundaries are evident in both cases, figures 24-26, intergranular and surface attack seems to be occurring in the latter cases. EDX examination of the surface of the unexposed specimen revealed no non-uniform distribution of nickel, chromium, or iron.

Plans: Specimens of Type 316 stainless steel will be evaluated under oxygen-rich conditions with a mixture of 80 percent by weight  $K_2CO_3$  with 20 percent by weight  $K_2SO_4$ . These specimens will be analyzed by SEM/EDX techniques. Further gravimetric and SEM/EDX analyses will be conducted on Type 304 stainless steels.

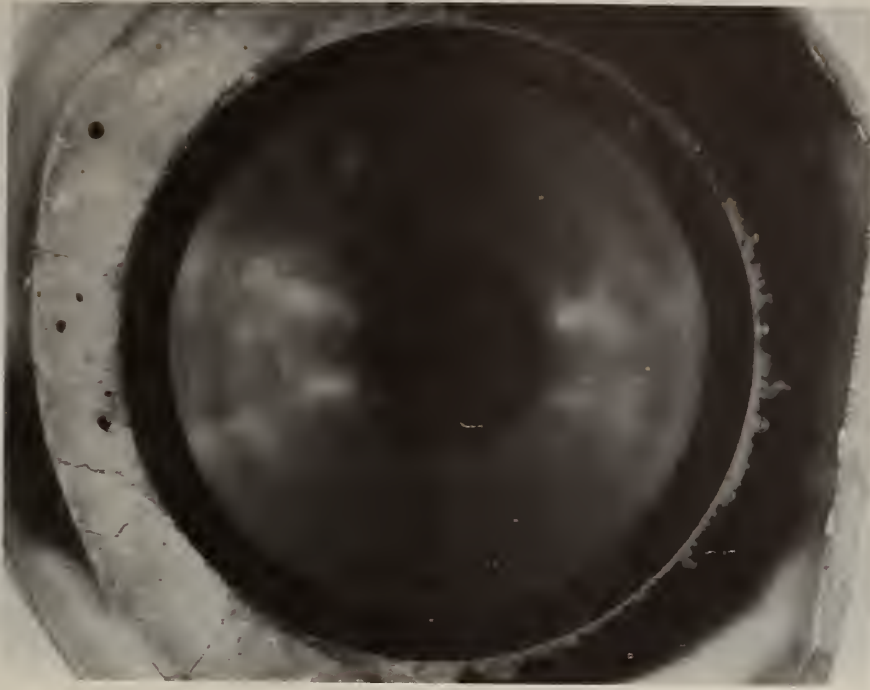


Fig. 1. Section of Type 316 stainless steel tubing after exposure to  $K_2SO_4$  seeded oxygen rich hot gas stream. Note formation of deposit on the upper surface. Tube temperature 590 °C.



Fig. 2. Section of Type 316 stainless steel tubing after exposure to  $K_2SO_4$  seeded oxygen rich hot gas stream. Note formation of deposit on the upper surface. Tube temperature 500 °C.



Fig. 3. Section of Type 316 stainless steel tubing after exposure to K<sub>2</sub>SO<sub>4</sub> seeded oxygen rich hot gas stream. Note formation of coating on the upper surface. Tube temperature 400 °C.



Fig. 4. SEM micrograph, 20 X, of K<sub>2</sub>SO<sub>4</sub> deposit on leading surface of Type 316 stainless steel. Specimen temperature 590 °C gas stream oxygen rich.



Fig. 5. SEM micrograph, 200 X, of gas stream-deposit interface showing potassium rich band.



Fig. 6. SEM micrograph, 500 X of Type 316 stainless steel-deposit interface. Specimen temperature 590 °C gas stream, oxygen rich.



Fig. 7. SEM micrograph, 2000 X, of center region of Fig. 6 showing reaction area at interface. Lettered regions correspond to labeled EDX spectra, Figs. 7a-7h. Specimen temperature 590 °C, gas stream oxygen rich.

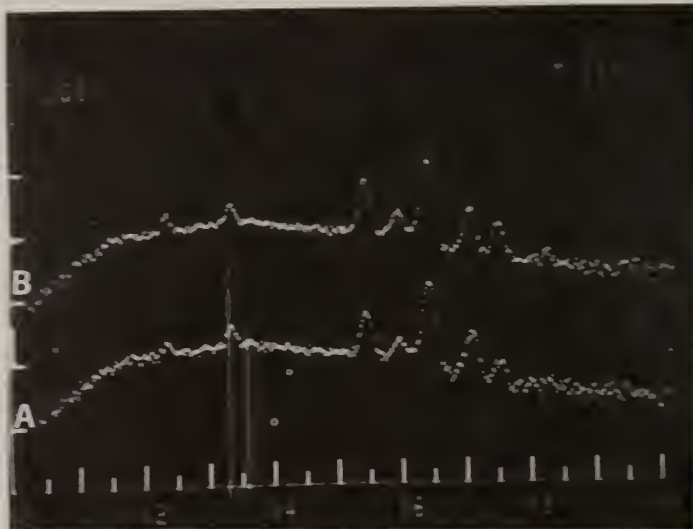


Fig. 7a. EDX spectra of regions A and B of Fig. 7 showing low Ni concentration areas. Specie positions and designations on all spectra in this section of this report are as indicated above.

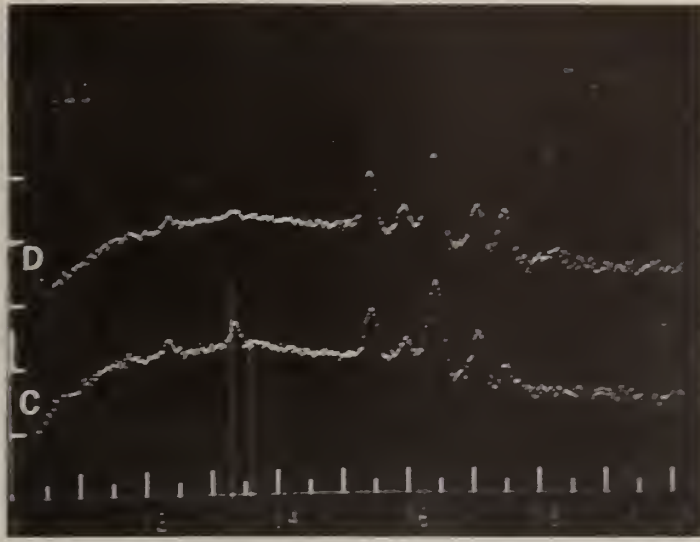


Fig. 7b. EDX spectra of regions C and D of Fig. 7 showing low Cr and low Ni concentrations in the reaction zone.

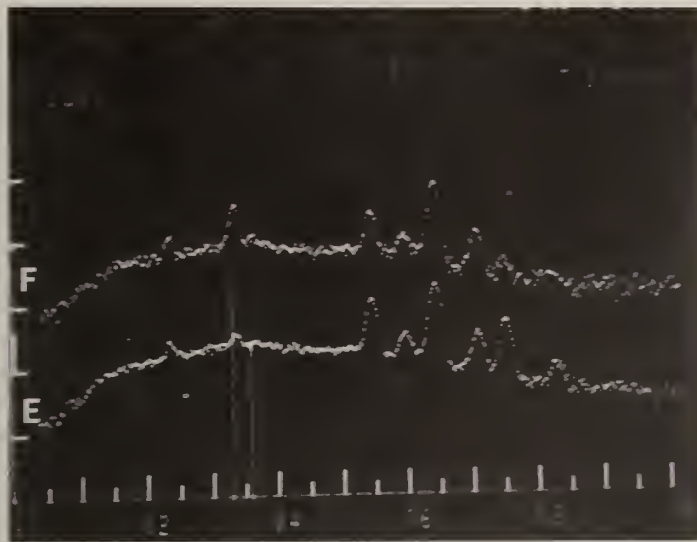


Fig. 7c. EDX spectra of regions E and F of Fig. 7 showing high Ni and low Cr concentrations.

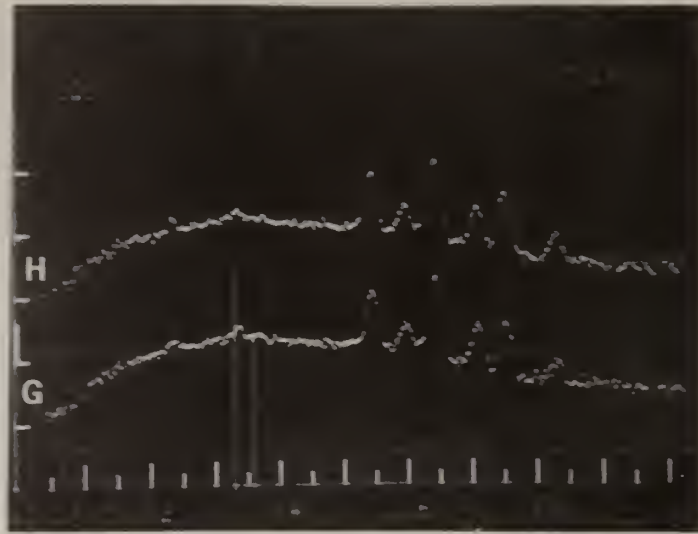


Fig. 7d. EDX spectra of regions G and H of Fig. 7 showing high Ni at the metal edge.

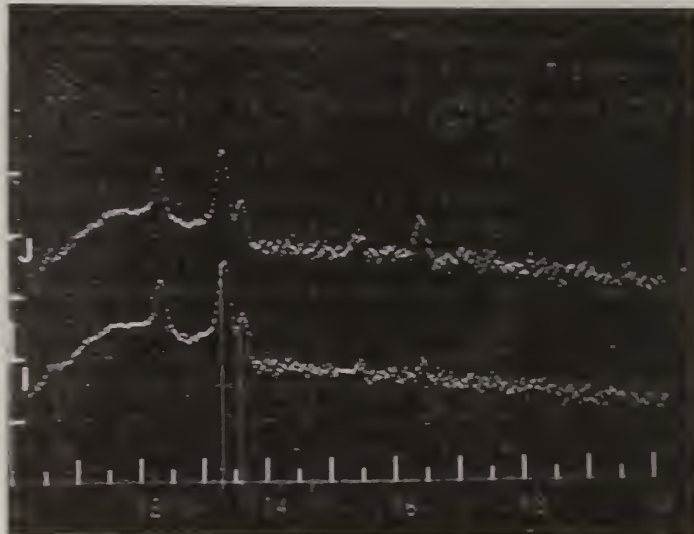


Fig. 7e. EDX spectra of regions I and J of Fig. 7 showing Fe penetration into the deposit.

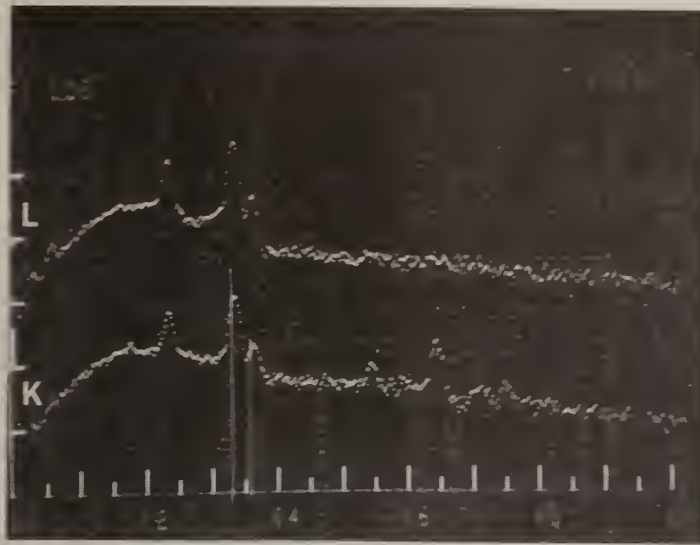


Fig. 7f. EDX spectra of regions K and L of Fig. 7 showing Fe and Cr penetration into the deposit.

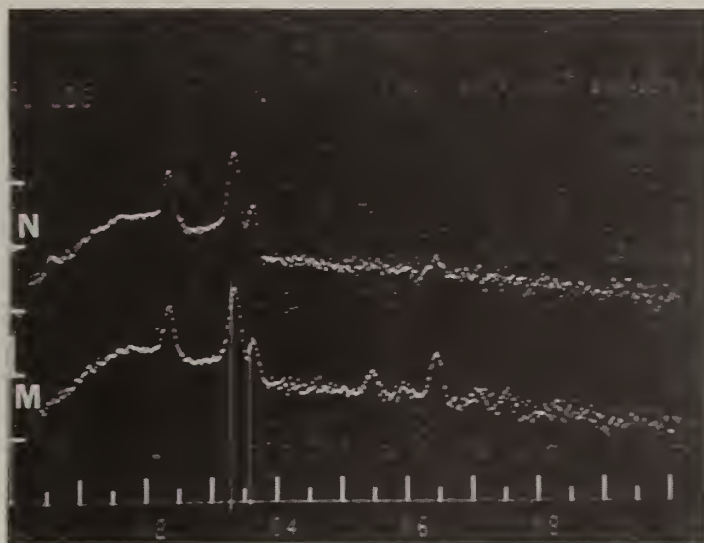


Fig. 7g. EDX spectra of regions M and N of Fig. 7 showing again Fe and Cr penetration into the potassium-sulfur deposit.

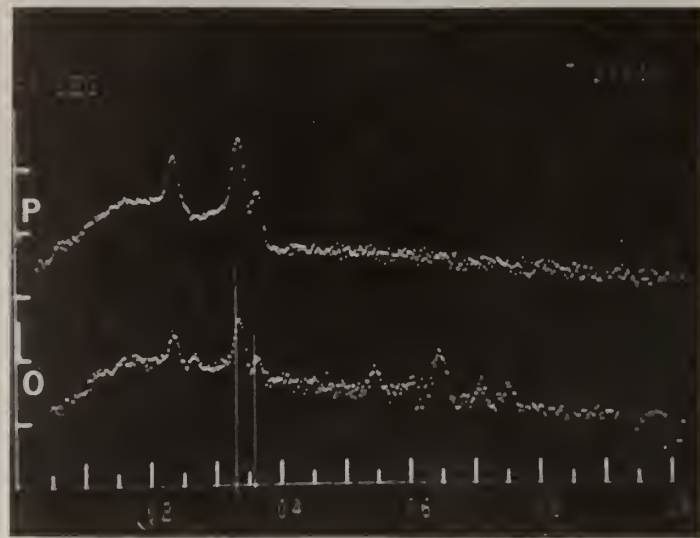


Fig. 7h. EDX spectra of regions O and P of Fig. 7 showing penetration of all three species, Fe and Cr and Ni into the deposit.

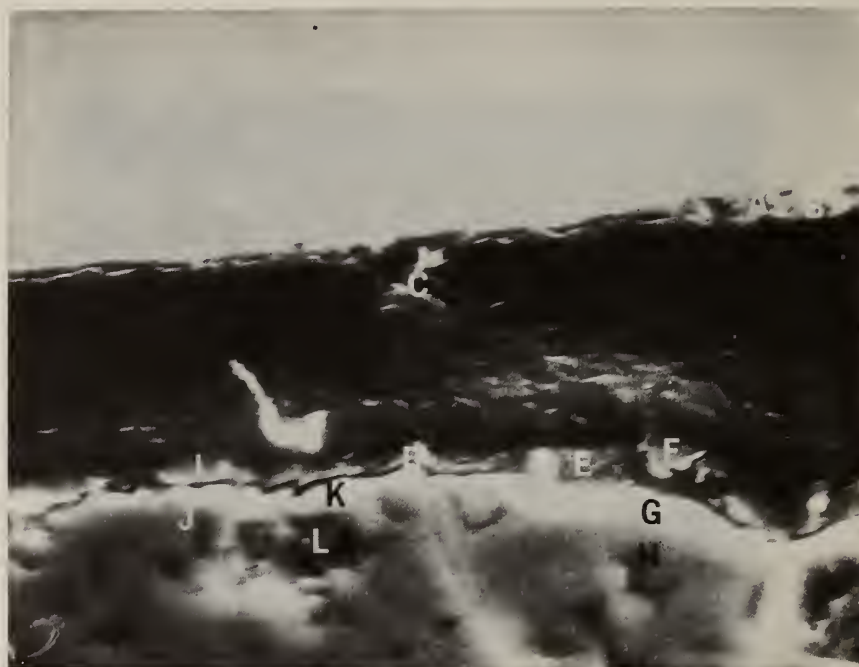


Fig. 8. SEM micrograph, 2000 X, of Type 316 stainless steel-deposit interface. Lettered regions correspond to labeled EDX spectra, Figs. 8a-8e. Specimen temperature 590 °C, gas stream oxygen rich.

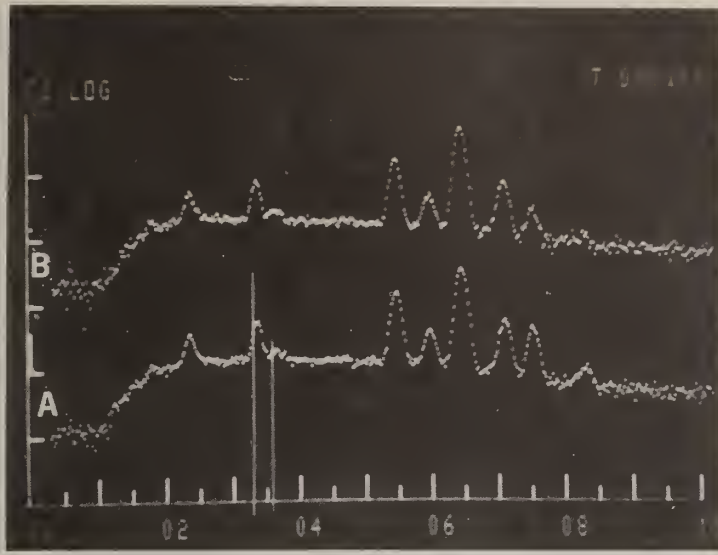


Fig. 8a. EDX spectra of regions A and B of Fig. 8 showing low Ni and low Cr concentrations at the metal edge.

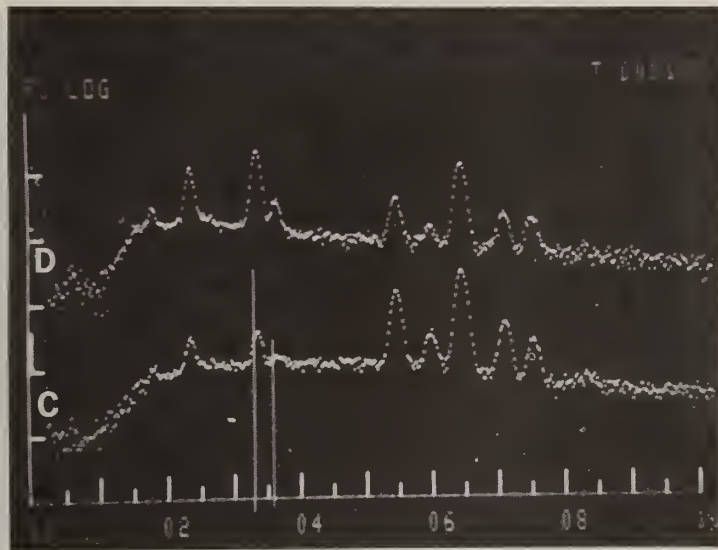


Fig. 8b. EDX spectra of regions C and D of Fig. 8 showing low Ni and low Cr concentrations at the metal edge.

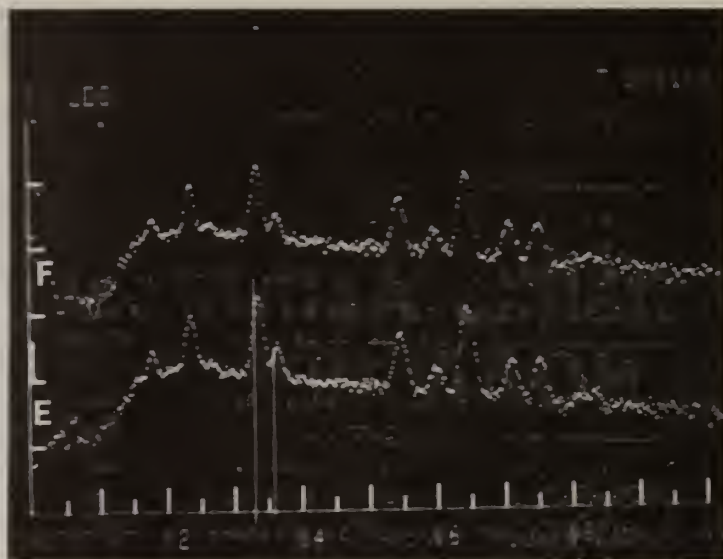


Fig. 8c. EDX spectra of regions E and F of Fig. 8 showing metal cations in the reaction zone of the deposit.

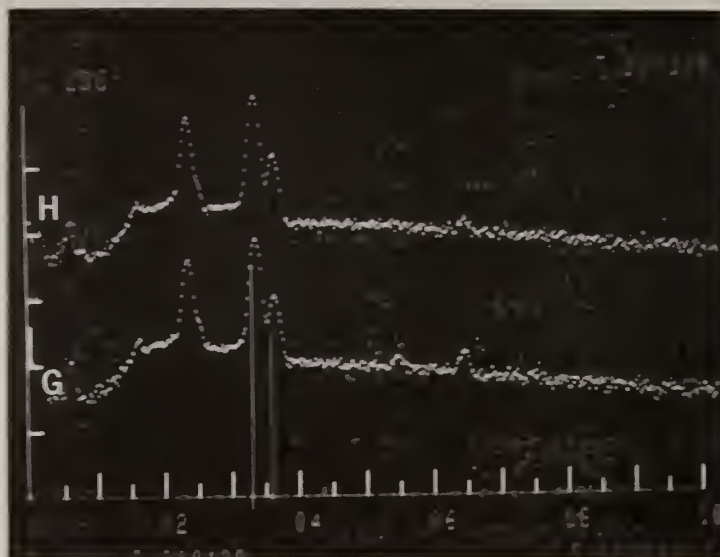


Fig. 8d. EDX spectra of regions G and H of Fig. 8 showing metal cations in the reaction zone of the deposit.

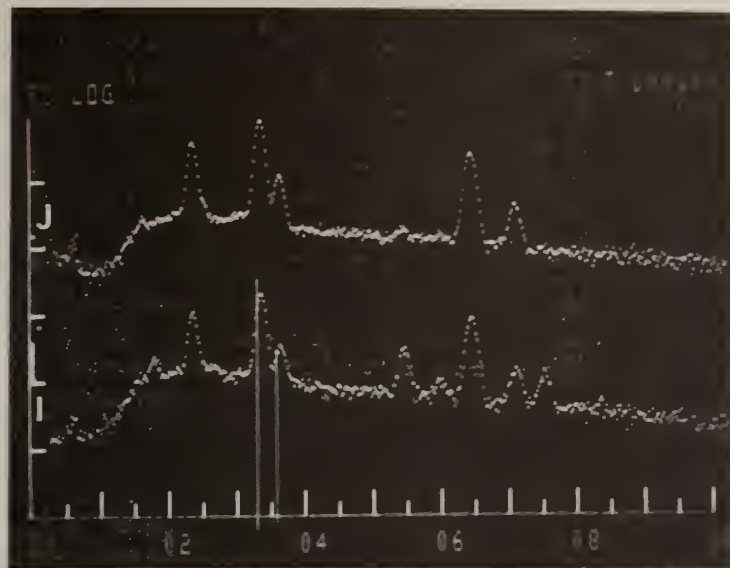


Fig. 8e. EDX spectra of regions I and J of Fig. 8 showing metal cations in the reaction zone of the deposit.

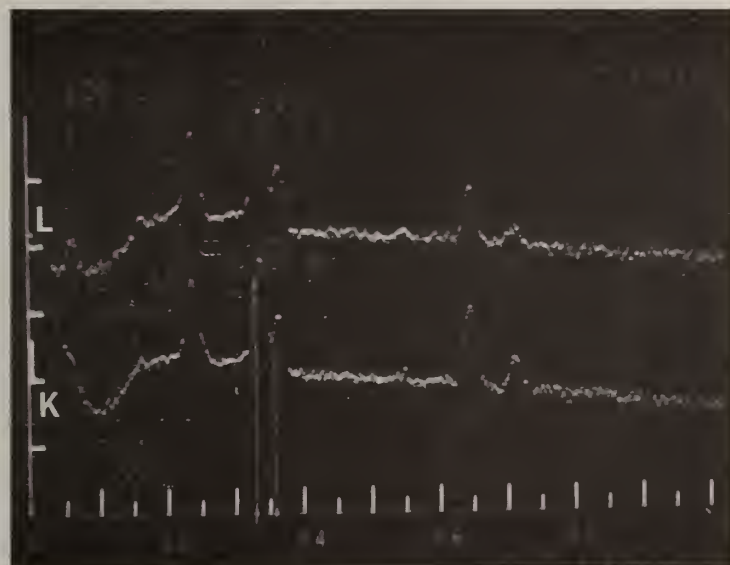


Fig. 9. EDX spectra of regions K and L of Fig. 8 showing Fe farther back in the deposit.

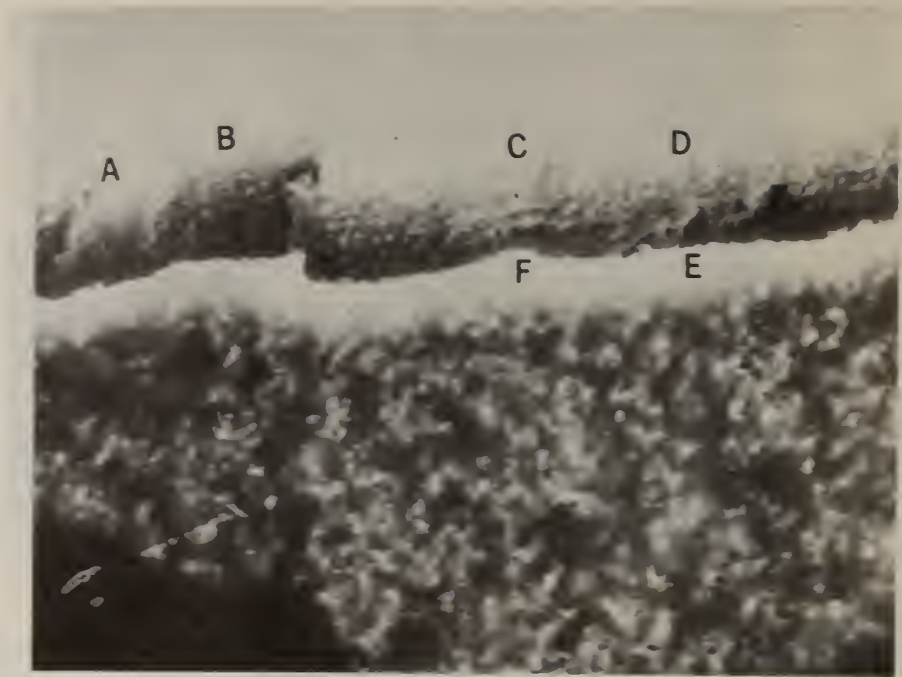


Fig. 10. SEM micrograph, 2000 X, of Type 316 stainless steel-fume deposit interface. Lettered regions correspond to labeled EDX spectra Figs. 10a-10c.

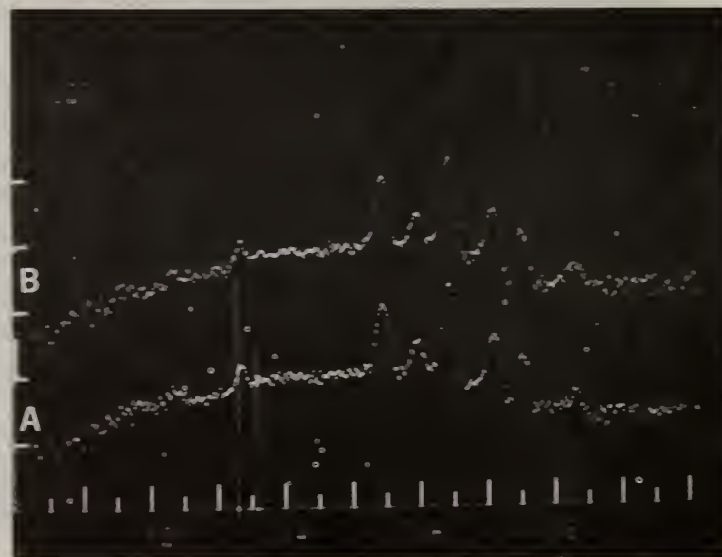


Fig. 10a. EDX spectra of regions A and B of Fig. 10 showing distribution of Cr, Fe and Ni at the stainless steel edge.

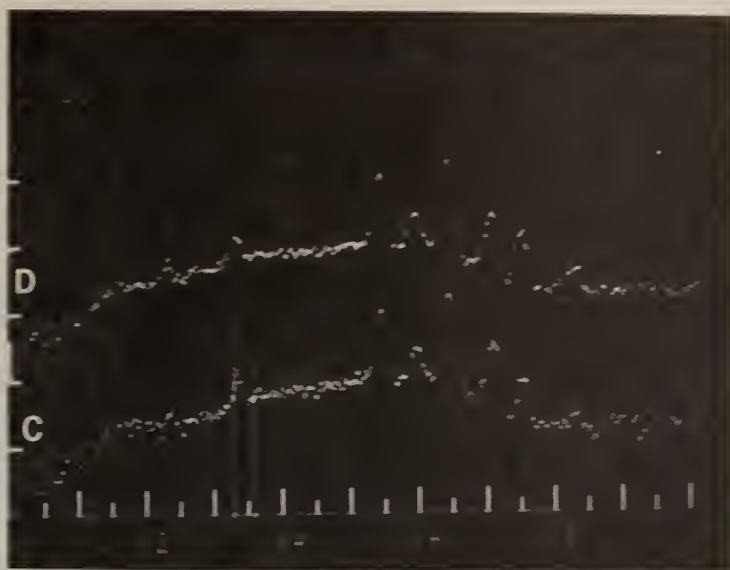


Fig. 10b. EDX spectra of regions C and D of Fig. 10 showing distribution of Cr, Fe and Ni at the stainless steel edge.

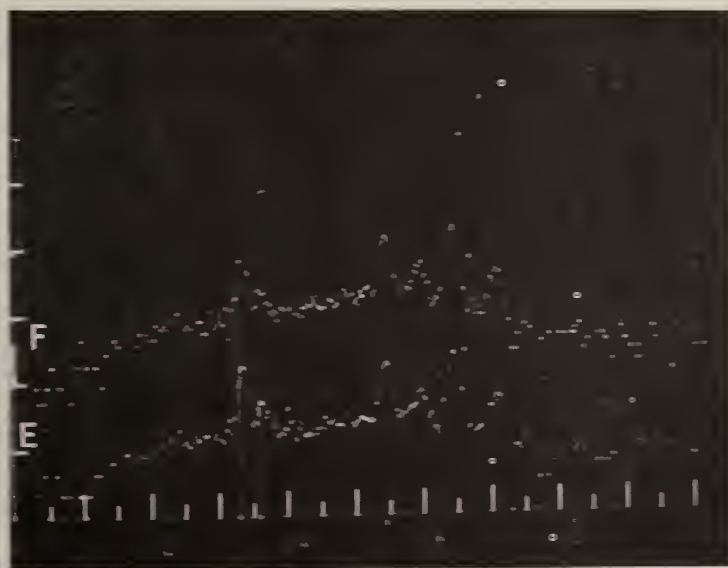


Fig. 10c. EDX spectra of regions E and F of Fig. 10 showing absence of Ni in the reaction zone.



Fig. 11. SEM micrograph, 2000 X of Type 316 stainless steel-deposit interface. Lettered regions correspond to labeled EDX spectra Figs. 11a-11h. Specimen temperature 500 °C, gas stream oxygen rich.

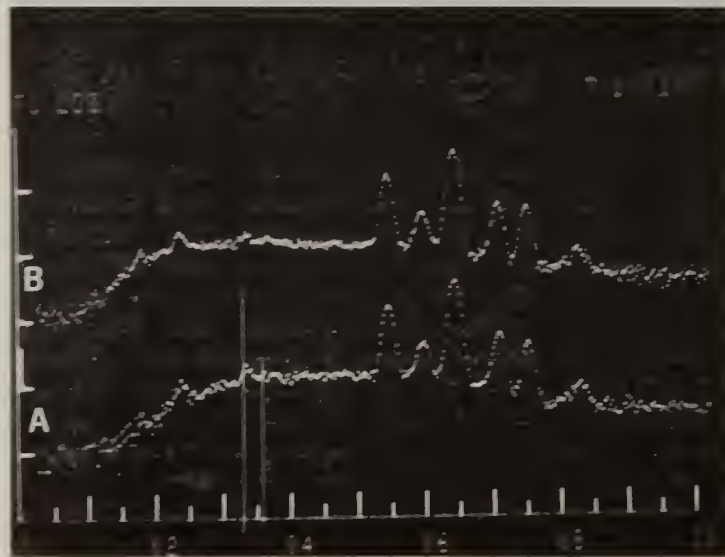


Fig. 11a. EDX spectra of regions A and B of Fig. 11 showing slight loss of Ni at stainless steel edge as compared to the bulk.

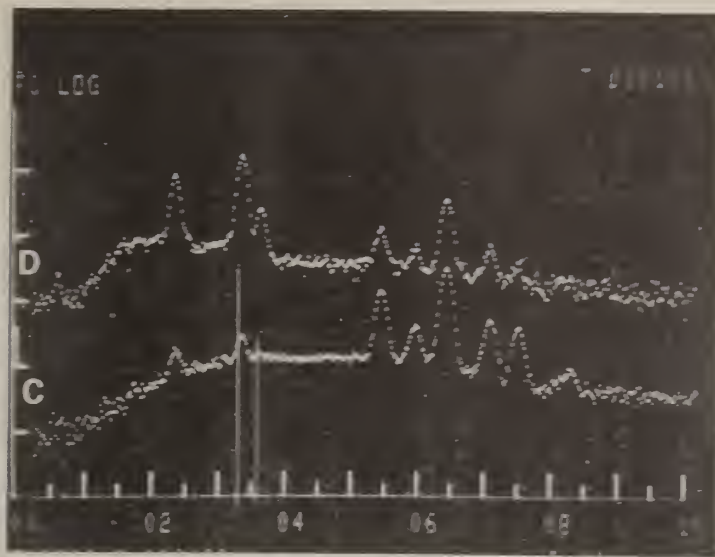


Fig. 11b. EDX spectra of regions C and D of Fig. 11 showing high Fe and low Cr and Ni concentrations in reaction zone.

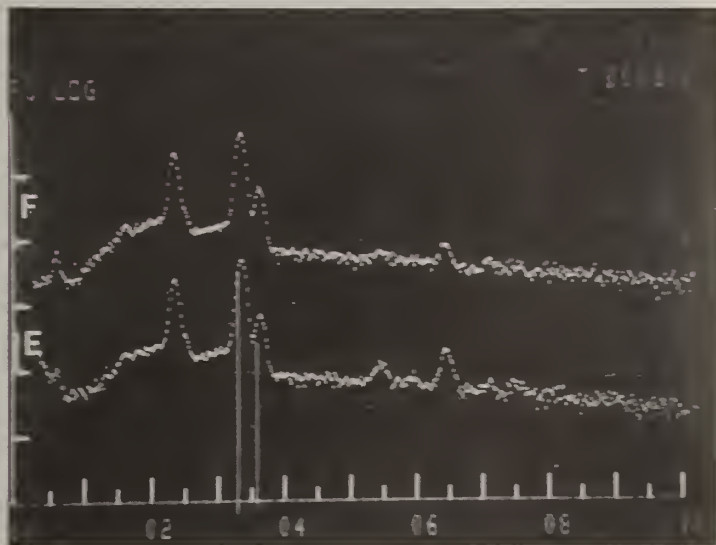


Fig. 11c. EDX spectra of regions E and F of Fig. 11 showing the penetration of Fe in the deposit.

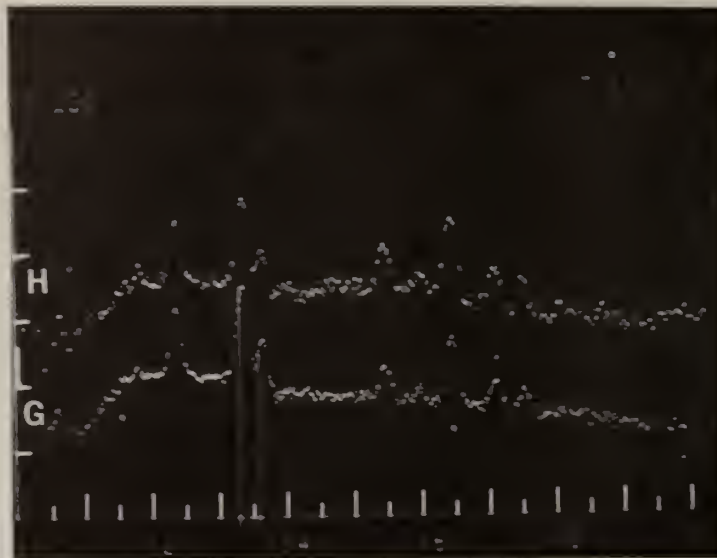


Fig. 11d. EDX spectra of regions G and H of Fig. 11 showing concentrations of Fe, Cr and Ni in the reaction zone of the stainless steel-deposit interface.

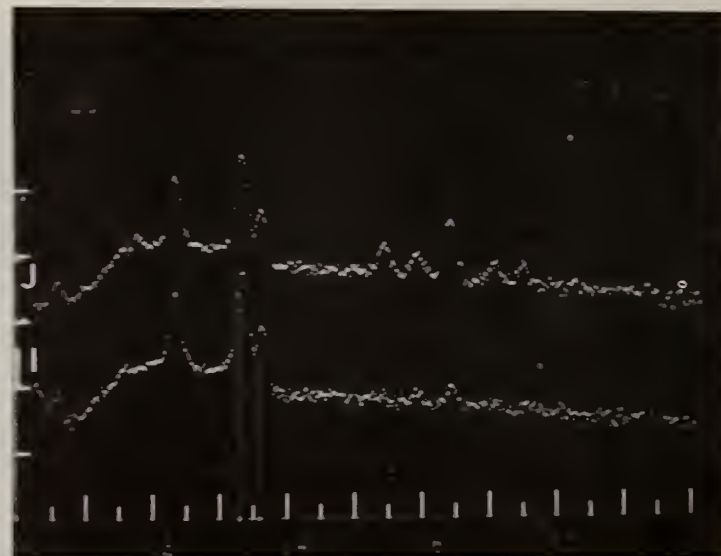


Fig. 11e. EDX spectra of regions I and J of Fig. 11 showing penetration of Fe, Cr and Ni in the deposit.

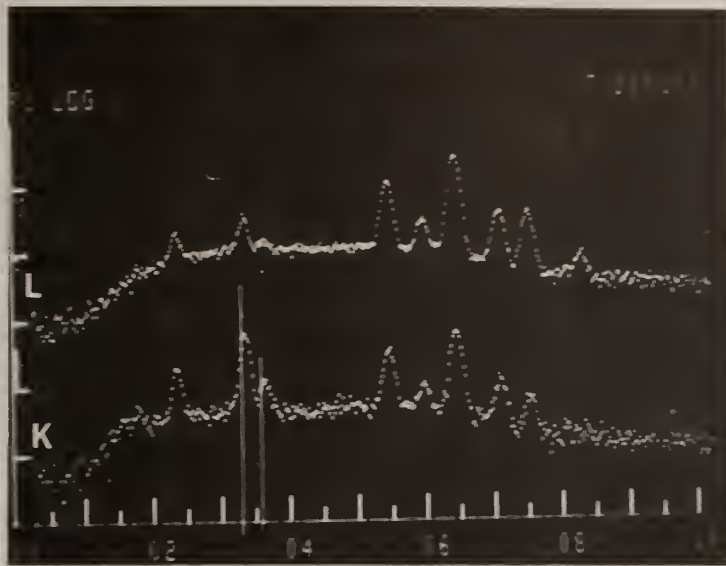


Fig. 11f. EDX spectra of regions K and L of Fig. 11 showing concentration of Fe, Cr and Ni at the metal edge.

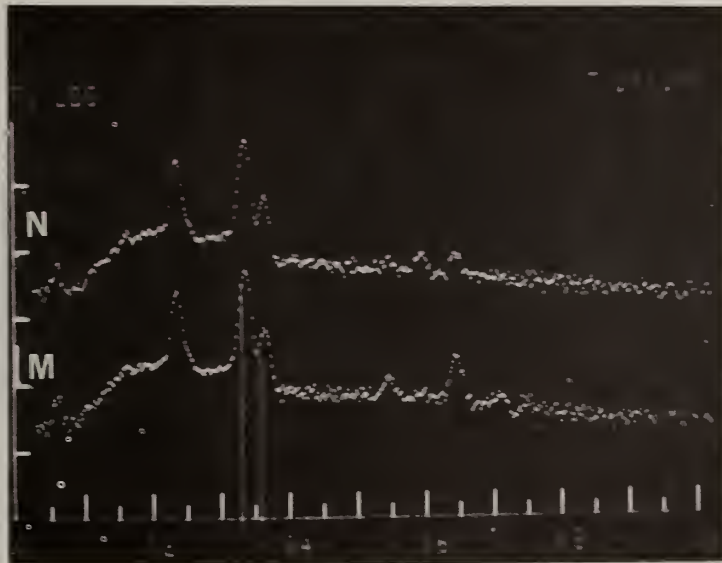


Fig. 11g. EDX spectra of regions M and N of Fig. 11 showing low concentration of Fe in reaction zone.

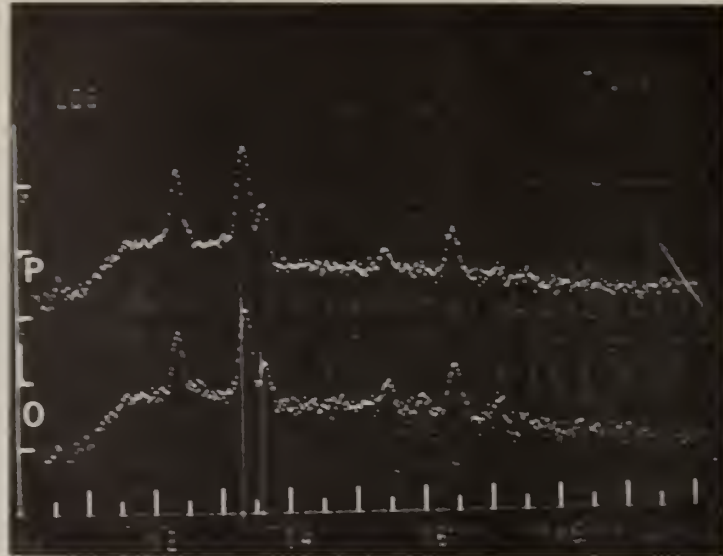


Fig. 11h. EDX spectra of regions O and P of Fig. 11 showing concentrations of Fe, Cr and Ni in the reaction zone.



Fig. 12. Type 316 stainless steel after exposure for 4 hours at 590 °C to K<sub>2</sub>SO<sub>4</sub> seeded, oxygen rich hot gas stream and subsequent cleaning. Approximately 2 X.



Fig. 13. Type 304 stainless steel after exposure for 4 hours at 590 °C to  $K_2SO_4$  seeded, oxygen rich hot gas stream and subsequent cleaning. Approximately 2 X.



Fig. 14. Type 304 stainless steel after exposure for 4 hours at 400 °C to  $K_2SO_4$  seeded, oxygen rich hot gas stream and subsequent cleaning. Approximately 2 X.

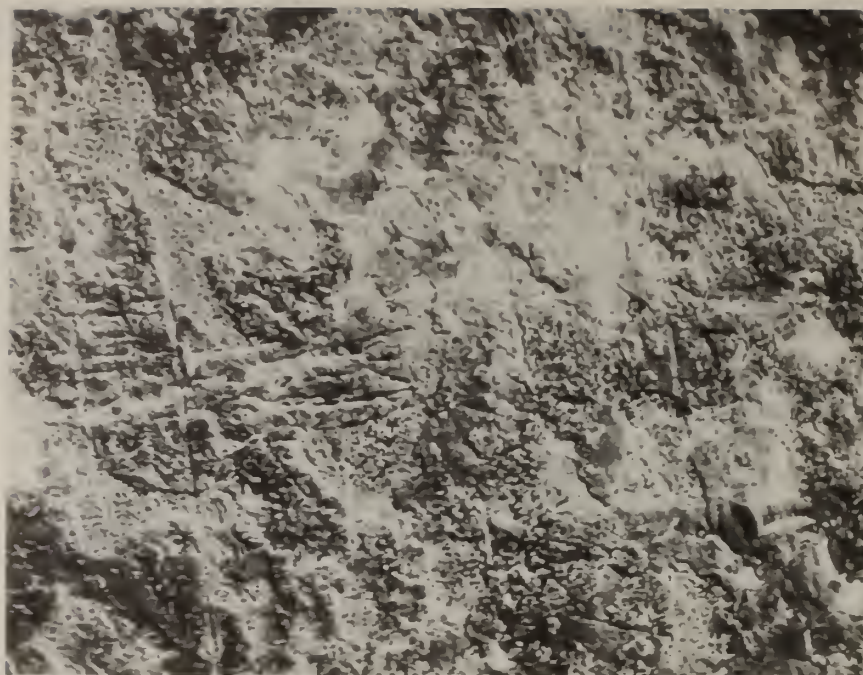


Fig. 15. SEM micrograph, 400 X, of Type 316 stainless steel exposed for 4 hours at 590 °C to  $K_2SO_4$  seeded, oxygen rich hot gas stream.



Fig. 16. SEM micrograph, 1600 X, of mid region of Fig. 15 showing surface attack.

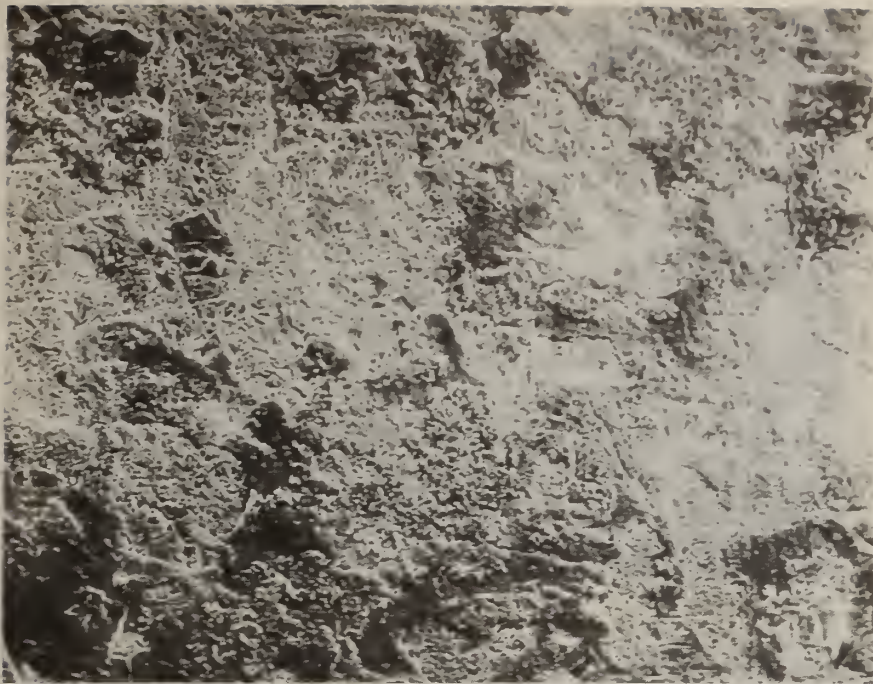


Fig. 17. SEM micrograph, 400 X, of Type 316 stainless steel exposed for 4 hours at 590 °C to  $K_2SO_4$  seeded, oxygen rich hot gas stream.

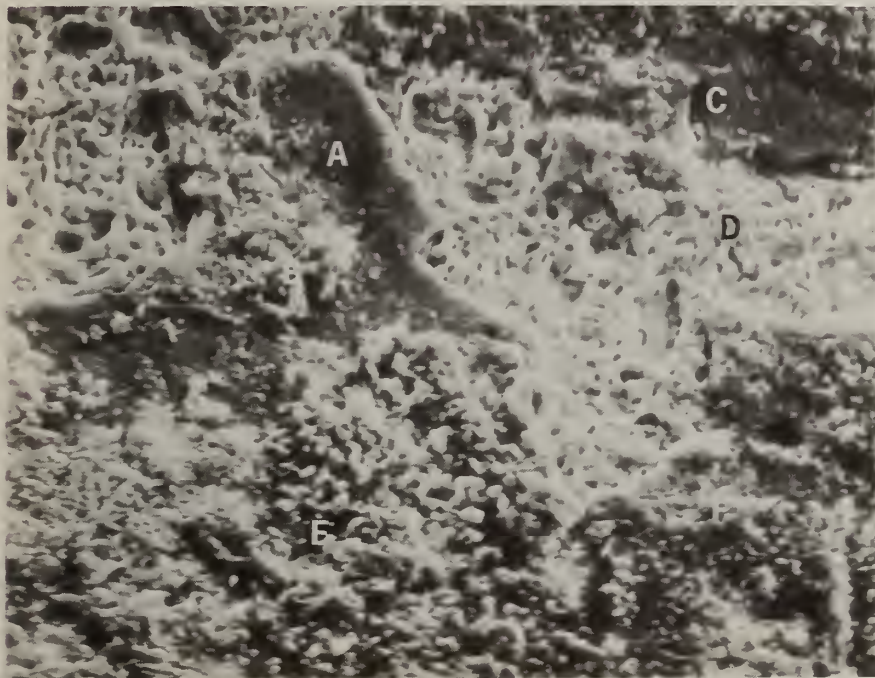


Fig. 18. SEM micrograph, 1600 X, of mid region of Fig. 17 showing surface attack. Labeled regions correspond to labeled EDX spectra, Figs. 18a-18c.

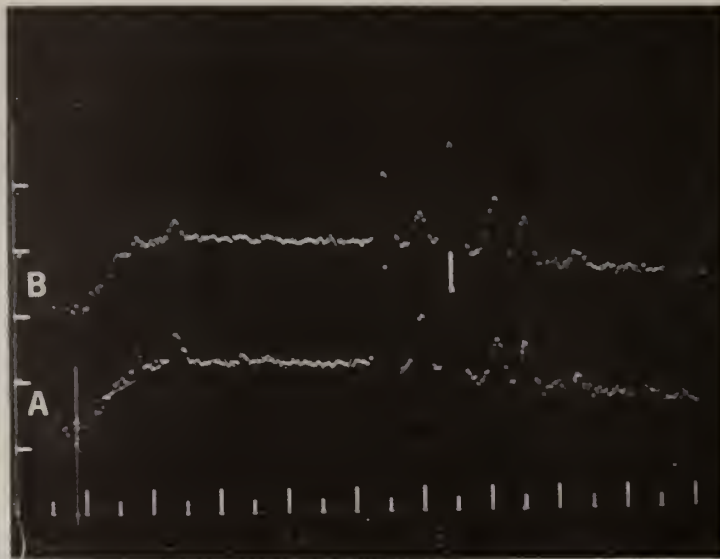


Fig. 18a. EDX spectra of regions A and B of Fig. 18 showing low Ni and high Cr concentrations.

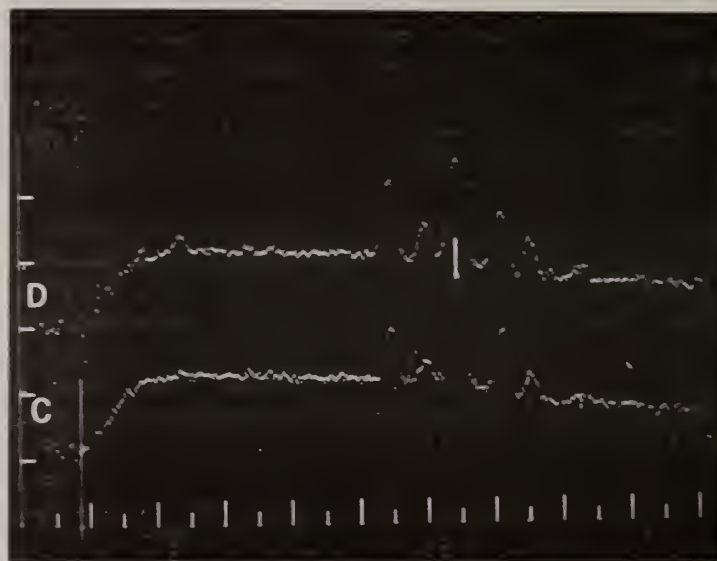


Fig. 18b. EDX spectra of regions C and D of Fig. 18 showing high Ni and high Cr concentrations.

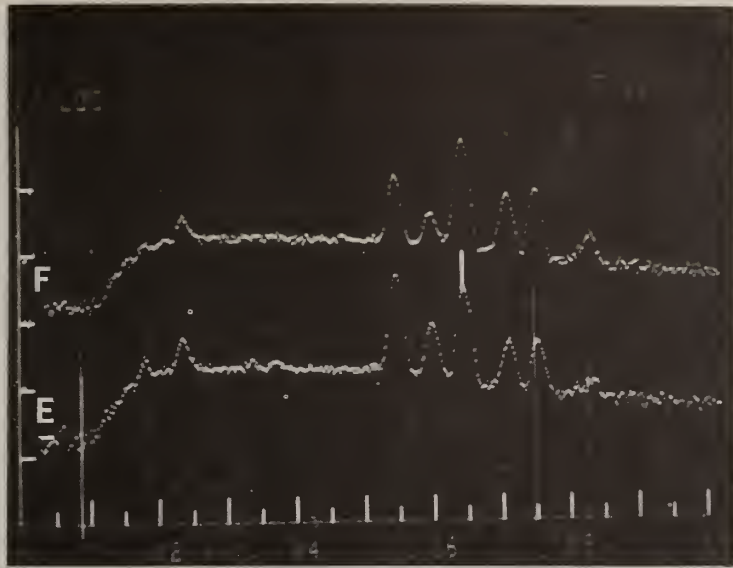


Fig. 18c. EDX spectra of regions E and F of Fig. 18 showing low Ni and high Fe concentrations.

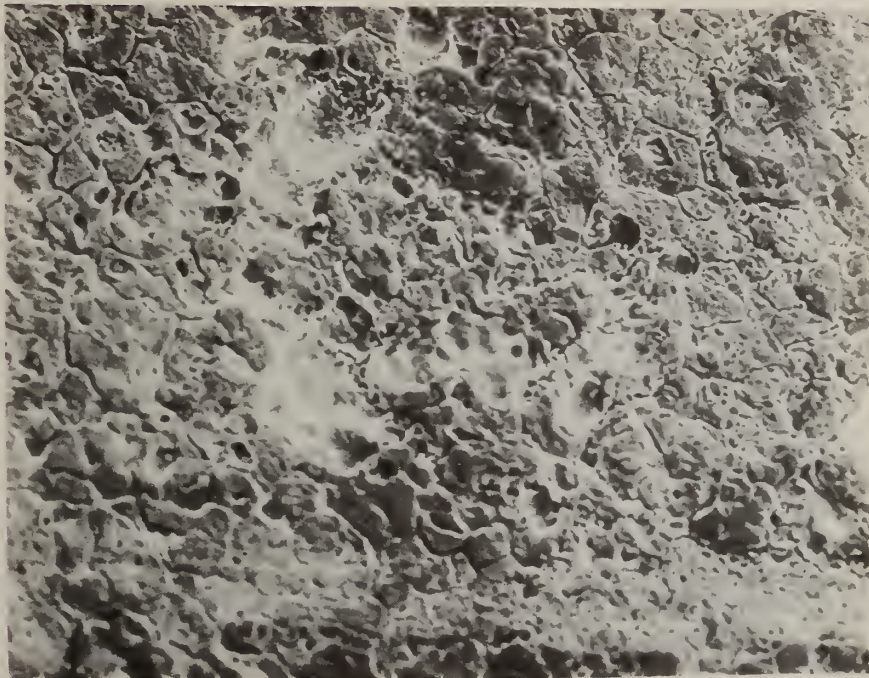


Fig. 19. SEM micrograph, 450 X, of Type 304 stainless steel exposed for 4 hours at 590 °C to a  $K_2SO_4$  seeded, oxygen rich hot gas stream.

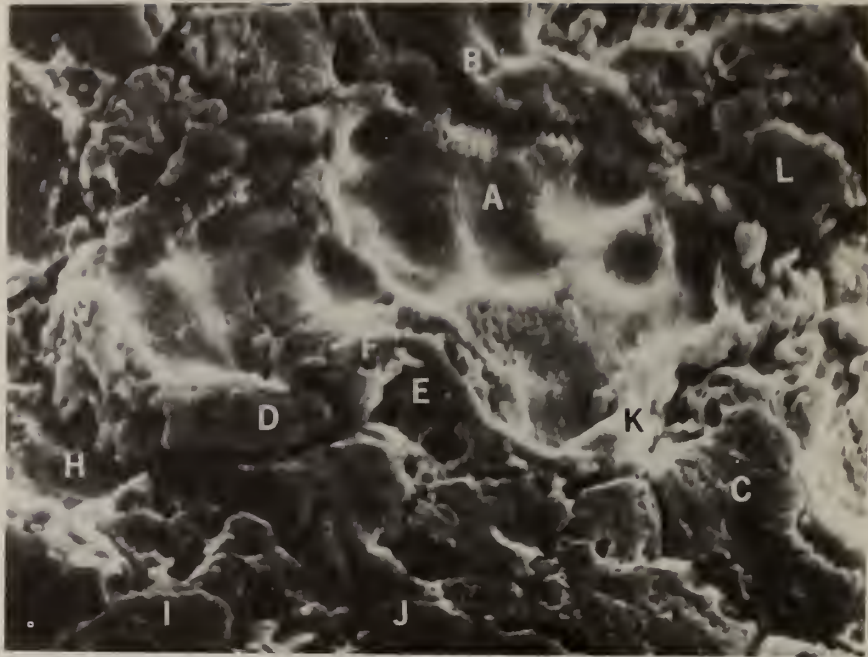


Fig. 20. SEM micrograph, 1900 X, of the mid region of Fig. 19 showing surface attack. Labeled regions correspond to labeled EDX spectra, Figs. 20a-20f.

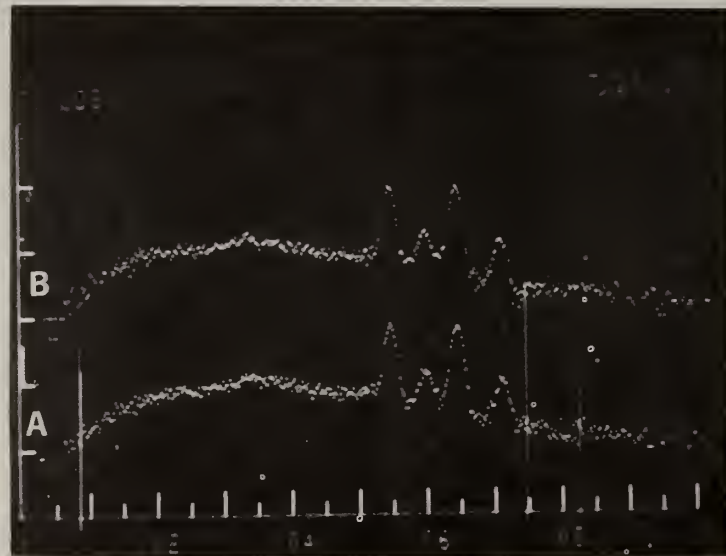


Fig. 20a. EDX spectra of regions A and B of Fig. 20 showing Ni depleted regions.

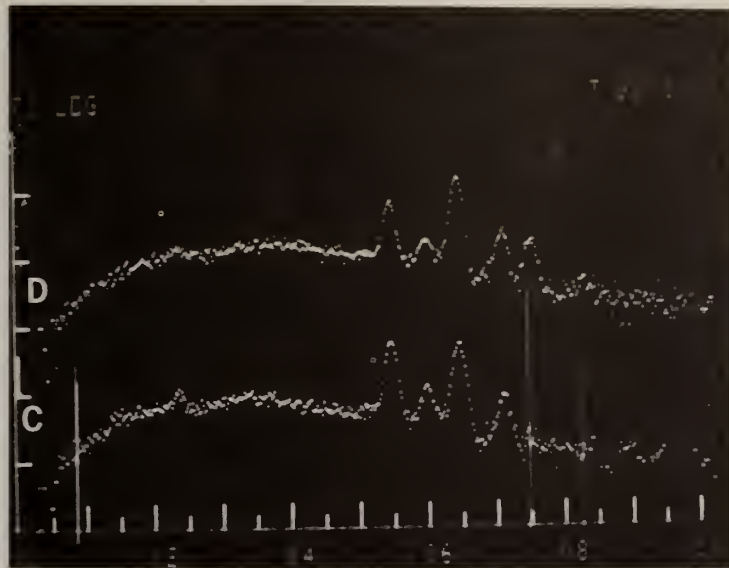


Fig. 20b. EDX spectra of regions C and D of Fig. 20 showing another Ni depleted region.

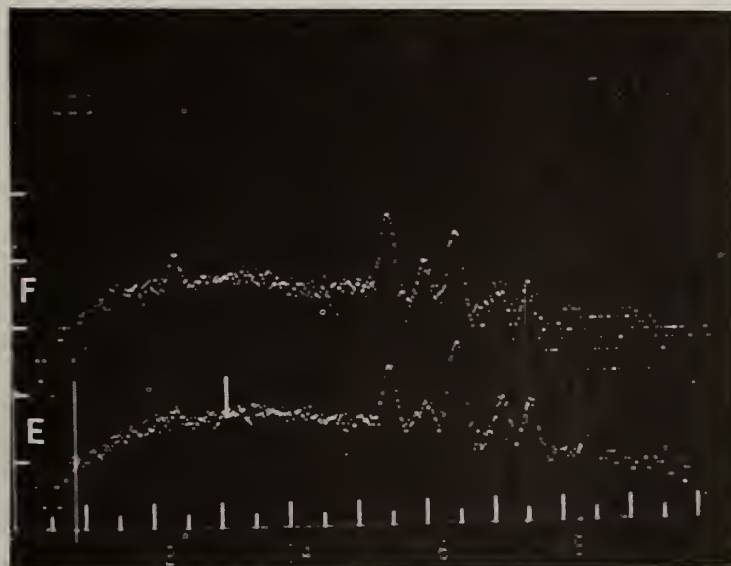


Fig. 20c. EDX spectra of regions E and F of Fig. 20 showing a region of high Cr concentration.

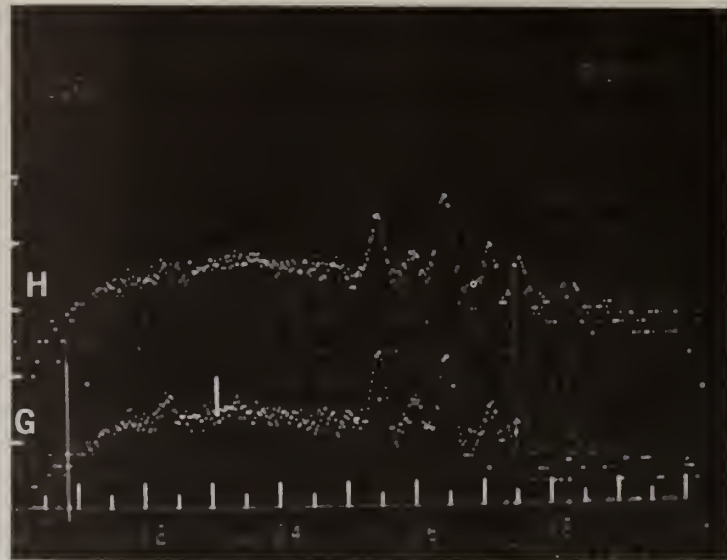


Fig. 20d. EDX spectra of regions G and H of Fig. 20 showing another region of high Cr concentration.

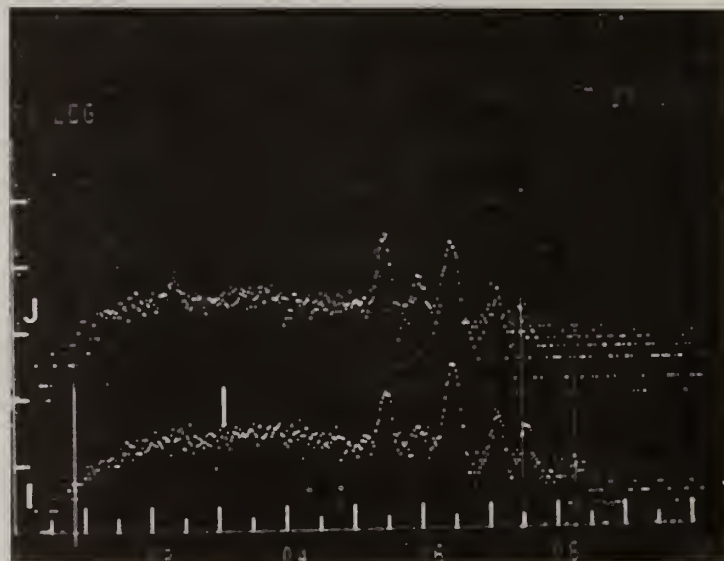


Fig. 20e. EDX spectra of regions I and J of Fig. 20 showing another region of high Cr concentration.

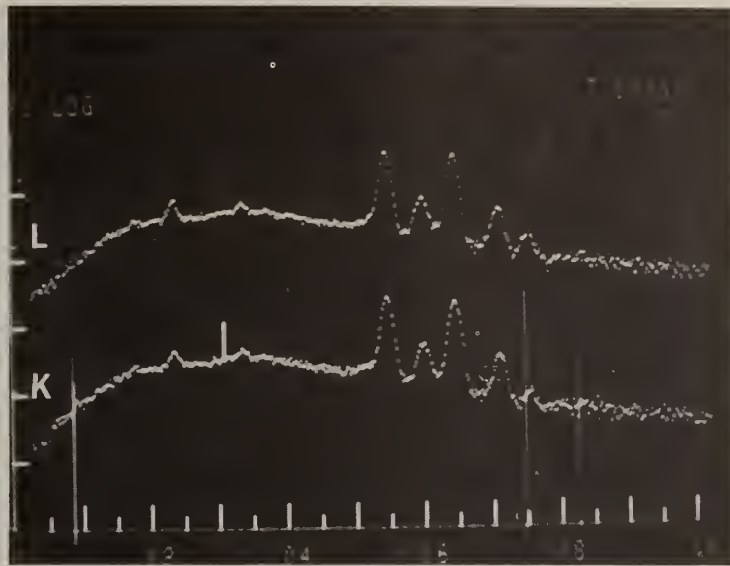


Fig. 20f. EDX spectra of regions K and L of Fig. 20 showing regions of high Cr and low Ni concentrations.

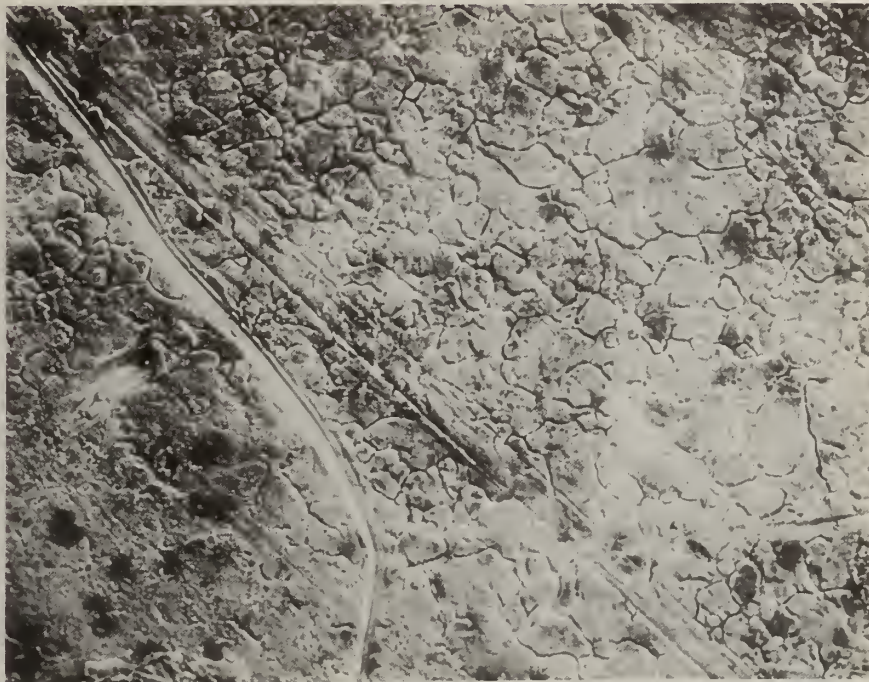


Fig. 21. SEM micrograph, 350 X, of Type 304 stainless steel specimen 14-4, exposed for 4 hours to a  $K_2SO_4$  seeded oxygen rich hot gas stream.



Fig. 22. SEM micrograph, 375 X, of another region specimen 14-4 showing what appears to be the onset of corrosion.

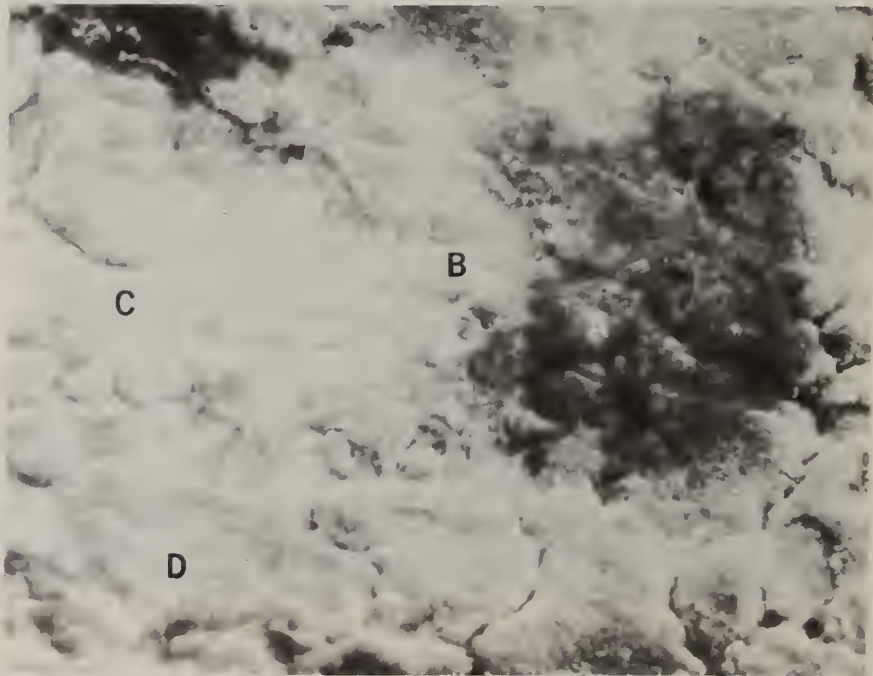


Fig. 23. SEM micrograph, 1500 X, of the mid region of Fig. 22. Labeled regions correspond to labeled EDX spectra, Figs. 23a and 23b.

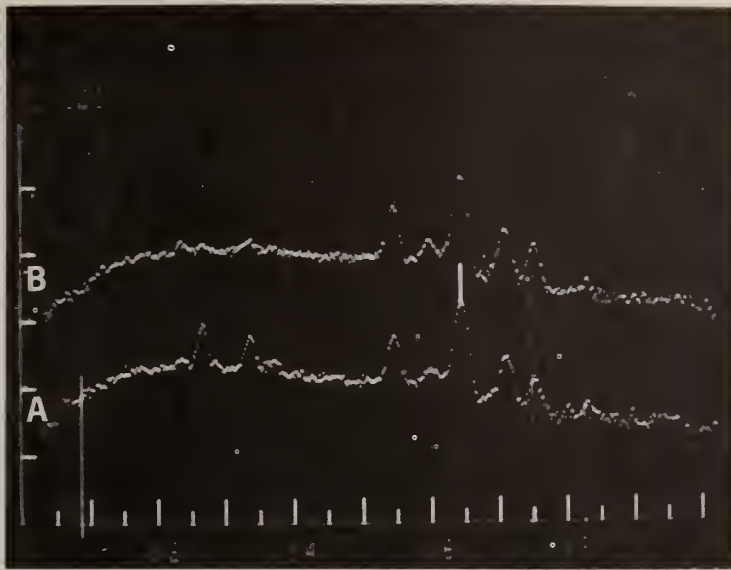


Fig. 23a. EDX spectra of regions A and B of Fig. 23 showing nickel depletion in a dark region.

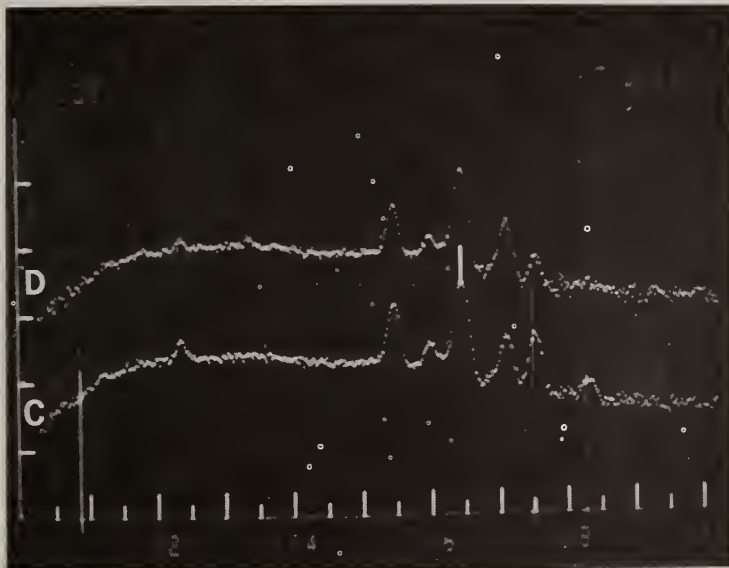


Fig. 23b. EDX spectra of regions C and D of Fig. 23 showing a Ni depleted region C and a region of high Ni and high Cr concentration, as well as low Cr.



Fig. 24. SEM micrograph of Type 304 stainless steel, unexposed but cleaned. Note grains and grain boundaries, 1600 X.



Fig. 25. SEM micrograph, 1900 X, of Type 304 stainless steel after exposure for 4 hours at 590 °C to a K<sub>2</sub>SO<sub>4</sub> seeded hot gas stream and subsequent cleaning. Note grain boundaries and grain surface.



Fig. 26. SEM micrograph, 1400 X, of Type 304 stainless steel after exposure for 4 hours at 400 °C to a  $K_2SO_4$  seeded hot gas stream and subsequent cleaning. Note grain boundaries and grain surface.

